The Effects of an Optic Field on the Anchoring Energies of Azo Dye-doped Liquid Crystals



Christopher Brennan

Department of Physics

Allegheny College

Meadville, Pennsylvania

April, 2013

The Effects of an Optic Field on the Anchoring Energies of Azo Dye-doped Liquid Crystals

Christopher Brennan

Senior Comprehensive Project

Spring 2013

Submitted to the Allegheny College

Department of Physics

to partially fulfill requirements for the degree of

Bachelor of Science

Committee Members:

Dr. David Statman

Dr. Daniel Willey

I hereby recognize and pledge to fulfill my responsibilities, as defined by the Honor Code, and to maintain the integrity of both myself and the College community as a whole.

Pledge: _____

Christopher Brennan

Acknowledgements

Dr. David Statman: You helped me through every aspect of this project, and I want to thank you for your patience and support along the way.

Dr. Daniel Willey: I started as a machine shop novice and became Bob the Builder in one semester. I couldn't have done it without you.

Cole: Your music and artwork brought culture to the lab and served as a constant inspiration. Also, your it'll-probably-be-fine attitude kept me from having panic attacks, which I consider a good thing.

Marla: I want to thank you for putting up with my silly questions throughout the semester. It's hard to believe you managed to write your own comp. with me nagging your ear off.

Sarah: Late-night comping would've been a drag if you weren't suffering right beside me. Thank you for keeping me sane during those fun times.

Brittany: I now know who to call if I ever have a chemistry-related question again. Thank you so much for all your help. I think now is the appropriate time to confess that about half of the minor fume hood infractions were my fault (sorry).

Abstract

This study investigates the effects of an optic field on azo-dye doped liquid crystals. It was anticipated that the photoexcitation of azo-dye altered surface conditions, which changed the anchoring coefficient of the liquid crystal. By measuring the changes in the second and third Stokes parameters, the extrapolation lengths were calculated both in the presence and absence of an optic field. The results were compared to observe how the anchoring energies changed under the influence of an optic field.

Contents

1 Introduction **6**

2 Background **7**

2.1 Liquid crystals 7

2.2 Electric and magnetic field effects 10

2.3 Distortion free energy 12

2.4 Birefringence 16

2.5 Azobenzene dyes 20

3 Theory **22**

4 Methodology **24**

4.1 Samples 24

4.2 Experimental Design 25

5 Results and discussion **29**

6 Conclusion **33**

7 Future work **34**

Appendices **36**

Appendix A Euler-Lagrange derivation **36**

Appendix B Sample preparation **38**

Appendix C Experimental procedure **40**

Appendix D Experimental Data **45**

D.1 Results 45

D.2 Calibrations 54

1 Introduction

The liquid crystal (LC) phase is a unique state of matter that occurs between the solid and liquid states. Austrian botanist Friedrich Reinitzer first observed this phase in 1888 while studying cholesterol in plants [1]. Upon further study, it was found that the phase exhibits certain characteristics that distinguish it from the solid and liquid states.

Perhaps the most unique characteristic of the LC phase is the tendency of the molecules to line up along a common axis called the director. This characteristic gives liquid crystals an anisotropic nature, meaning that they exhibit different properties when observed along different axes. An electric or magnetic field applied to a liquid crystal will exert a torque on the molecules causing reorientation of the director. The degree to which the molecules reorient depends on the strength of the interactions between the molecules and their boundaries. If the interactions at the boundaries are strong, then the molecules experience a smaller reorientation in response to an applied field. Because these interactions tend to keep the molecules in place, they are said to give the liquid crystal an anchoring energy.

The strength of this anchoring energy varies depending on the medium, and it may be subject to alterations. In the past, research has compared the photoinduced gliding effect and the anchoring energy of liquid crystals infused with the azo-dyes disperse orange 3 (DO3) and methyl red (MR). This was done by measuring the polarization of light that propagates through an irradiated liquid crystal sample for several intensities and polarizations of an incoming probe beam. The results showed that at the same polarization (+45 degrees) and intensity (15mW) MR oriented 14 degrees while DO3 oriented 0.25 degrees in the same amount of time. In addition, it was observed that

MR adsorbed a significantly greater amount of dye than DO3 upon irradiation [2].

The variations between the dyes could be a result of easy-axis gliding and/or the degree of anchoring at the surface [3][4]. The purpose of this research is to determine the impact of anchoring on director reorientation as opposed to the gliding effect. This is done by comparing the anchoring energies of various dye-doped liquid crystals before and after photoexcitation.

2 Background

2.1 Liquid crystals

As temperature increases matter undergoes phase transitions typically from solid to liquid; however, certain substances exhibit a phase that occurs between solid and liquid states called the liquid crystal phase. Since this phase occurs between the solid and liquid states, it follows that molecules in the liquid crystal phase demonstrate properties of both crystalline solids and liquids [1]. In a crystalline solid state, the molecules both point along a specific direction and occupy specific sites on a lattice, which demonstrates both orientational and positional order. On the other hand, the molecules in the liquid state flow freely and randomly with respect to one another, which demonstrates a lack of both orientational and positional order. This suggests that molecules in the liquid crystal phase lie somewhere in the middle of ordered and disordered. As it turns out, molecules in the liquid crystal phase exhibit no positional order, like a liquid, but have a certain degree of orientational order, like a solid.

This orientational order stems from the fact that the molecules, while flowing about, tend to spend more time lined up along a specific direction as opposed to any other

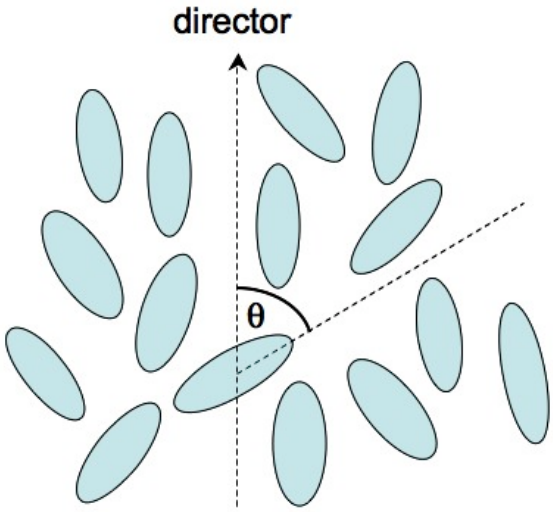


Figure 1: An illustration of the director in a liquid crystal. Specifically, this diagram represents the director of a calamitic liquid crystal in the nematic phase [1].

direction. The amount of orientational order in a liquid crystal depends on the degree to which each of the molecules deviate from this preferred direction, referred to as the director. The deviation from the director is described by the angle θ formed between the primary axis of the liquid crystal molecules and the director as shown in Figure 1.

Since the orientation of the liquid crystal molecules is not a constant in time, an order parameter is defined. The most useful formulation of the order parameter is described by the average of the second Legendre polynomial given by

$$S = \langle P_2(\cos\theta)\rangle = \langle \frac{3\cos^2\theta - 1}{2}\rangle. \tag{1}$$

where S is the order parameter and the brackets denote an average over many molecules at the same time [1]. Representing the order parameter in this way yields S=1 for a perfectly ordered sample and S=0 for a completely disordered sample. Liquid crystals typically have order parameters ranging from 0.3 to 0.8 that can be calculated in many ways including the measurement of diamagnetism or optical birefriengence of a liquid

crystal sample.

The orientational order varies depending on the type of liquid crystal. Some types of liquid crystals include discotic, calamitic, and bent-core. Each of these liquid crys-

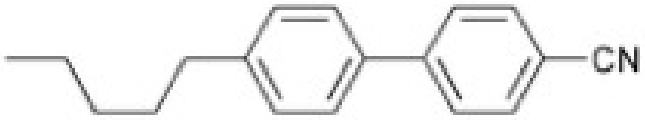


Figure 2: Typical calamitic liquid crystal molecule [1].

tal types can exist in different phases such as isotropic, nematic, smectic, and chiral nematic, which are characterized by the type of ordering. This study utilizes calamitic liquid crystals in the nematic phase.

A typical calamitic liquid crystal is characterized by two or more carbon ring stuctures joined together by a rigid linking group with hydrocarbon chains at each end as shown in Figure 2. The rigid linking group is responsible for the elongated shape

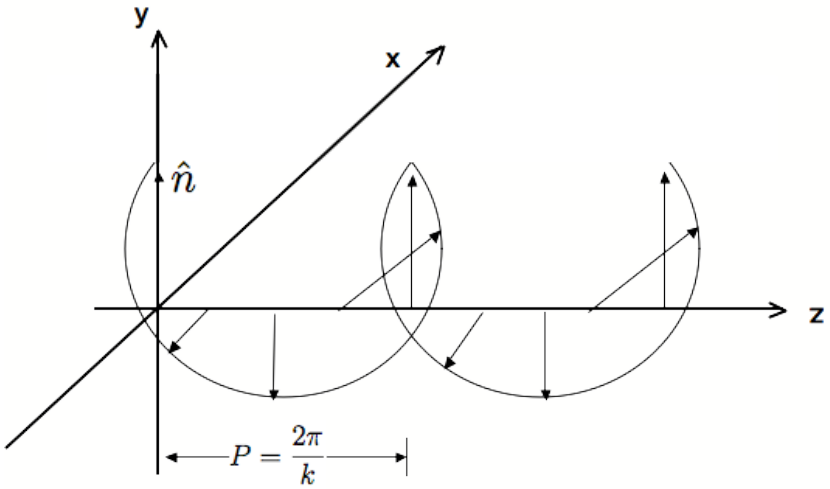


Figure 3: A depiction of director behavior in a chiral nematic liquid crystal. Note that the pitch length of the helix is denoted by P [5].

giving the molecules a uniaxial property; that is, molecules with one axis much longer than the other two [1].

In the nematic phase, these rod-like molecules exhibit a high degree of orientational order, which results in a distinct, unidirectional director as shown in Figure 1.

In the chiral nematic phase, the director varies in a helical pattern throughout, as shown in the Figure 3, where the pitch length P is used to describe the distance required for the director to perform one complete turn. As will be discussed, the pitch length is important for describing a twist geometry that is induced within a nematic liquid crystal.

2.2 Electric and magnetic field effects

The application of a field, either electric or magnetic, changes the orientation of the director within a liquid crystal. By inducing a dipole on the liquid crystal molecules, a field can exert a torque on each molecule causing it to rotate into the direction of the applied field. For an electric field, the torque per volume is given by

$$\vec{N_v} = \vec{P} \times \vec{E} \tag{2}$$

where $\vec{P}$ is the induced polarization, or dipole moment per unit volume, of the liquid crystal. The induced polarization depends linearly on the electric field, but the anisotropy of the liquid crystal causes the polarization to vary depending on the axis. To account for this, the induced polarization is represented as

$$\vec{P} = \varepsilon_0 \chi_e \vec{E} \tag{3}$$

where ε_0 is the permittivity of free space and χ_e is the dielectric susceptibility tensor of the molecule. In this way, each component of the electric field corresponds to the

different values of χ_e along the respective axes. The components of the electric field are given as

$$E_{\parallel} = \vec{E} \cdot \hat{n}$$

$$E_{\perp} = |\vec{E} - (\hat{n} \cdot \vec{E})\hat{n}|. \tag{4}$$

Note that these components are parallel and perpendicular to director denoted $\hat{n}$ respectively. From this, the polarization of the molecule can be written as

$$\vec{P} = \varepsilon_0[\chi_{e\perp}\vec{E} + (\chi_{e\parallel} - \chi_{e\perp})(\hat{n} \cdot \vec{E})\hat{n}] \tag{5}$$

where $\chi_{e\parallel}$ and $\chi_{e\perp}$ are the parallel and perpendicular components of the dielectric susceptibility. Therefore the torque exerted on the nematic becomes

$$\vec{N} = \varepsilon_0(\chi_{e\parallel} - \chi_{e\perp})(\hat{n} \cdot \vec{E})(\hat{n} \times \vec{E}) \tag{6}$$

which reduces to

$$N = \frac{1}{2}\Delta\chi_e\varepsilon_0 E^2 \sin(2\varphi) \tag{7}$$

where φ is the angle between the director and the applied electric field. For a magnetic field, H, $\Delta\chi_e$ and ε_0 are replaced by the magnetic anisotropy $\Delta\chi_m$ and the magnetic permeability μ_0 respectively.

Analysis of Eq. 7 suggests that the maximum torque occurs when the field is applied 45 degrees with respect to the director. Furthermore, it suggests that the net torque is zero when the field is applied perpendicular to the director. Even though the net torque is zero for a perpendicularly applied field, it does not mean that the director

can never rotate. In fact, for a perpendicularly applied field, rotation can occur above a threshold field strength, referred to as the Freédericksz threshold.

Above the Freédericksz threshold field, the director starts to rotate from its undistorted configuration toward the direction of the electric field. This occurs because the destabilizing torques arising due to dielectric anisotropy become strong enough to overcome the anchoring energies at the boundaries.

2.3 Distortion free energy

The field-induced rotations of the director result in three types of distortions, which are shown in Figure 4. The energies corresponding to each distortion are analogous to the energy of a spring. Each distortion energy is proportional to the square of the spatial derivative of the director, just as the energy of the spring is proportional to the square of the change in equilibrium postion. As a result, the field-induced distortions can be expressed by a free energy per unit volume given by

$$F_v = \frac{1}{2}K_1[\nabla \cdot \hat{n}]^2 + \frac{1}{2}K_2[\hat{n} \cdot (\nabla \times \hat{n})]^2 + \frac{1}{2}K_3[\hat{n} \times (\nabla \times \hat{n})]^2 \tag{8}$$

where K_1, K_2, and K_3 are constants corresponding splay, twist, and bend respectively [1]. Just as a spring-constant describes the stiffness of the spring, these constants describe the stiffness of the director; that is, how resistant it is to the motion caused by each distortion. As it turns out, the boundaries play a significant role in determining the types of distortions that result, which makes Eq. 8 incomplete.

For this study, the boundaries consist of two PI-coated pieces of glass rubbed in one direction. In order to understand the effects of these boundaries, consider an electric

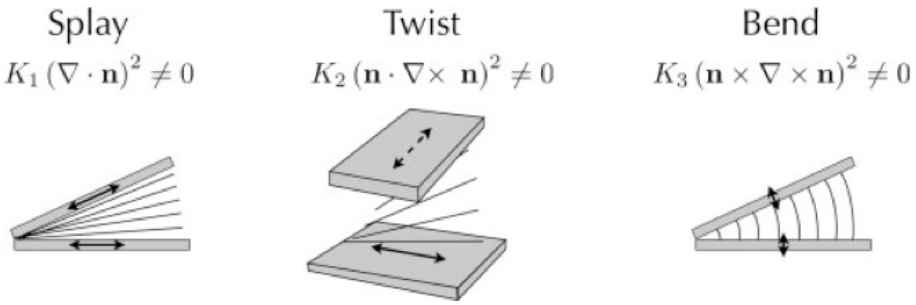


Figure 4: A depiction of the three classifications of distortion in liquid crystals and their corresponding energies [15].

field that is applied perpendicular to the rubbing direction on a nematic liquid crystal sample cell as shown in the Figure 5.

The electric field causes the director to rotate from its equilibrium position by an angle φ. Due to the boundary conditions, an energy will constrain the director to point along the x-axis giving $\varphi = 0$ at each surface. This suggests that along the z-axis φ will increase from 0, reach a maximum at $z = L/2$, and then decrease unitl it reaches 0 again at $z = L$. Since the angle of the director varies along the z-axis, the liquid

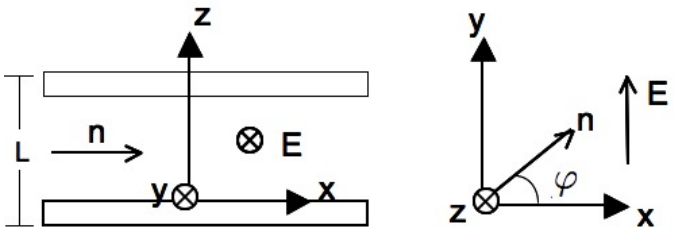


Figure 5: Depiction of the liquid crystal sample geometry that results in a twist distortion, where φ represents the change in the director from equilibrium [1].

crystal experiences distortion. The distortion can be described by the components of the director, which for this case are

$$n_x = \cos[\varphi(z)]$$

$$n_y = \sin[\varphi(z)]. \tag{9}$$

Evaluating these components in Eq. 8 yields

$$\nabla \cdot \hat{n} = 0$$

$$\hat{n} \cdot (\nabla \times \hat{n}) = -n_x \left(\frac{\partial n_y}{\partial z} \right)_{x,y} + n_y \left(\frac{\partial n_x}{\partial z} \right)_{x,y} = -\frac{d\varphi}{dz} \tag{10}$$

$$(\hat{n} \times (\nabla \times \hat{n})_z = n_x \left(\frac{\partial n_x}{\partial z} \right)_{x,y} + n_y \left(\frac{\partial n_y}{\partial z} \right)_{x,y} = 0$$

suggesting that the distortion within the sample is pure twist. It is important to note that the particular application of the field shown in Figure 5 results in only one type of distortion. Consequently, pure splay and bend distortions can be achieved by perpendicularly applying a field along other orientations. However, for this study, only twist distortions were considered in order to minimize the zenithal energy of the sample.

The energy per area resulting from this field-induced twist is given by

$$U = \frac{1}{2} K_2 (\frac{d\varphi}{dz})^2 + \frac{1}{2} \varepsilon_0 \Delta\chi_e E^2 \sin^2 \varphi \tag{11}$$

where the first term corresponds to the twist distortion energy and the second term corresponds to the energy of the applied field. Integration of Eq. 11 from 0 to L gives the contributions of these energies throughout the sample, but it does not represent the total energy. The missing components are that of the anchoring energies, or the energies that constrain the motion of the director at each surface. These anchoring energies are given by the Rapini-Papoular form

$$W = \frac{1}{2} W_a \sin^2(\varphi - \varphi_e) \tag{12}$$

where W_a is the anchoring energy coefficient which is an intrinsic value of the polymer PI, φ is the director angle, and φ_e is the easy axis angle which corresponds to the director orientation that minimizes the anchoring energy [6].

The consideration of all energy contributions gives the total energy of the sample cell as the distortion free energy, F, per cross-sectional area,

$$F = \int_0^L [\frac{1}{2} K_2(\frac{\partial\varphi}{\partial z})^2 + \frac{1}{2}\eta\Delta\varepsilon\varepsilon_0\langle E^2\rangle \sin^2(\varphi-\varphi_E)]dz + \frac{1}{2}W_0 \sin^2(\varphi-\varphi_0) + \frac{1}{2}W_L \sin^2(\varphi-\varphi_L) \tag{13}$$

where φ is the azimuthal angle of the director, $\Delta\varepsilon$ is the dielectric anisotropy of the nematic, φ_E is the azimuthal angle of the field, and the brackets around the electric field E are a time average [7]. The constant η corresponds to a torque effect present in dye-doped liquid crystal samples and will be discussed later.

Minimizing the distortion free energy, F, describes the actual director configuration throughout the liquid crystal sample. This can be done using the method of Euler-Lagrange, as shown in Appendix A, which yeilds

$$\frac{d^2\varphi}{dz^2} = \frac{1}{2}\eta\langle E^2\rangle\frac{\Delta\varepsilon\varepsilon_0}{K_2}\sin[2(\varphi-\varphi_E)] \qquad \textit{bulk} \tag{14}$$

$$\frac{d\varphi}{dz} = -\frac{1}{2}\frac{W_e}{K_2}\sin[2(\varphi-\varphi_e)] \qquad \textit{surface};\ e{=}\ 0, L \tag{15}$$

In the absence of a field, $E = 0$, $\frac{d^2\varphi}{dz^2} = 0$ in the bulk, and the azimuthal angle is described by

$$\varphi = kz + c \tag{16}$$

where the constants c and k are determined by the boundary conditions from Eq. 15.

Since the pitch of the twist in a nematic is given by $P = 2\pi/k$, Eq. 16 can be substituted into Eq. 15 and evaluated at z=L to yield

$$\frac{2\pi}{P} = -\frac{1}{\xi}\sin\left[2\left(\frac{2\pi}{P}L - \varphi_L\right)\right] \tag{17}$$

where ξ is the extrapolation length equivalent to K_2/W_L. Here, the extrapolation length refers to the distance between the actual director orientation and the preferred orientation called the easy axis [1]. It is important to note that P, the twist in the nematic, is described by both the azimuthal angle of the easy axis and the extrapolation length. Since extrapolation length is inversely proportional to the anchoring coefficient W_L at the surface, Eq. 17, suggests that twist distortion results from a difference in actual director alignment and easy axis alignment as a result of anchoring conditions.

In the presence of a field, Eq. 14 is integrated to yield

$$\frac{d\varphi}{dz} = \sqrt{\frac{\eta\Delta\varepsilon\varepsilon_0}{K_2}\langle E^2\rangle}\sqrt{\sin^2(\varphi - \varphi_E) - \sin^2(\varphi_{max} - \varphi_E)} \tag{18}$$

where φ_{max} corresponds to the angle where $\frac{d\varphi}{dz} = 0$. As shown by Eq. 15, knowledge of the anchoring conditions is required in order to integrate Eq. 18. Therefore, when Eq. 18 is substituted into Eq. 15, the anchoring coefficient can be determined by varying the field strength and measuring φ and $d\varphi/dz$ at each surface [8].

2.4 Birefringence

The birefringence of nematic liquid crystals allows for the orientation of the director, φ, to be determined. Birefringence is the property of anisotropic materials that causes light to propagate through a medium at different speeds depending on the direction.

This occurs because the indices of refraction are not the same along different axes.

The uniaxial structure of a nematic, depicted in Figure 6, produces two different refractive indicies. These include the index for light polarized along the direction of the long-axis called the extraordinary index, n_e, and the index for light polarized perpendicular to this direction called the ordinary index, n_o. The anisotropy of the

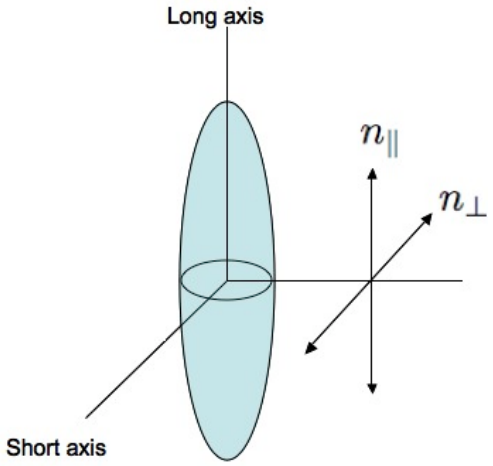


Figure 6: An illustration of the long and short axes of a calamitc liquid crystal and the corresponding ordinary and extaordinary polarization directions dentoed by $n_{\perp}$ and $n_{\parallel}$ respectively.

nematic is given by $\Delta n = (n_{\parallel} - n_{\perp})$, where $n_{\parallel}$ and $n_{\perp}$ are the indices of refraction for light polarized in the parallel and perpendicular directions respectively [1].

As light polarized in different directions propagates through the nematic, the parallel and perpendicular components of light will travel at different speeds. Thus the two components of light that enter the liquid crystal in phase grow out of phase as they propagate through the nematic. To account for this, a phase difference δ is introduced between the two components of light,

$$\delta = \frac{2\pi}{\lambda_0}\Delta n d = \Delta n k_0 d \tag{19}$$

where k_0 is the wavevector of the light in a vacuum and d is the thickness of the medium.

If $\delta = 0$ or $\pm\pi$, then the electromagnetic wave passing through the nematic is linearly polarized through some angle. If $\delta = \pm\pi/2$ and the amplitudes of each component are equal, then the wave is circularly polarized. And all other configurations of δ produce variations of elliptical polarization.

As it turns out, there is a special case for the propagation of light through a twisted nematic that minimizes the phase difference. This special case occurs when the pitch of the twist distortion is much greater than the wavelength, $P \gg \lambda_0$ [1]. When this condition is met, the orientation of the director changes very slightly over distances of several wavelengths. Therefore it is permitted to think of the light as propagating through slices of nematic liquid crystal with the orientation of the director changing slightly from slice to slice as shown in the Figure 7.

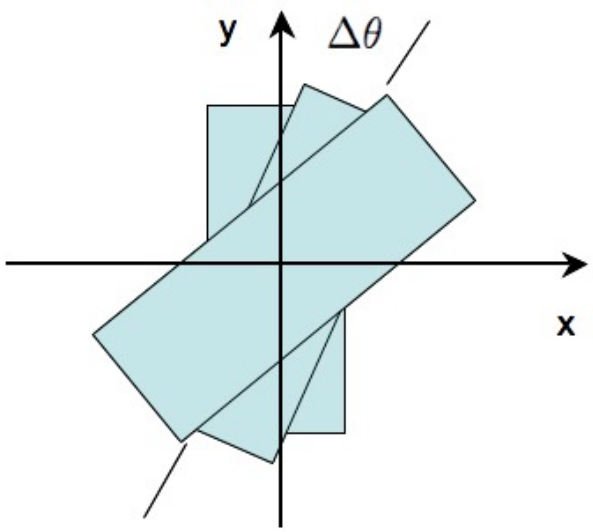


Figure 7: Nematic slices of a twist distorted liquid crystal [1].

If the thickness of each slice d is very small such that $P \gg \lambda_0 \gg d$, then it follows that the phase difference $\delta = \Delta n k_0 d$ of light passing through one slice is close to 0. Consequently, the light remains linearly polarized since it does not get out of phase when passing through each slice. However, the orientation of the director changes by

$\Delta\theta$ from slice to slice. Because of this, the electric field must be considered as having two components, one perpendicular to the director, $E_0 \sin(\Delta\theta)$, and the other parallel to the director, $E_0 \cos(\Delta\theta)$, when passing through the nematic. The resulting effect of each slice on the propagating light is to rotate the polarization direction by the same angle as the director rotates from slice to slice. As a result, the polarization of the light follows the director as it rotates throughout the sample for this special case.

The polarization of light following the director can be described using Stokes parameters, which are often combined into a vector known as Stokes vector:

$$\vec{S} = \begin{bmatrix} S_0 \\ S_1 \\ S_2 \\ S_3 \end{bmatrix} = \begin{bmatrix} I \\ Q \\ U \\ V \end{bmatrix} \tag{20}$$

where the initial Stokes parameter S_0 is intensity of the light, S_1 is linearly polarized light, S_2 is light polarized at 45 degrees, and S_3 is circularly polarized light. This can be rewritten in terms of the components of the applied light yielding

$$\begin{bmatrix} S_0 \\ S_1 \\ S_2 \\ S_3 \end{bmatrix} = \begin{bmatrix} I_0 \\ |E_x|^2 - |E_y|^2 \\ |E_{45}|^2 - |E_{-45}|^2 \\ |E_{left}|^2 - |E_{right}|^2 \end{bmatrix} \tag{21}$$

where I_0 is the intensity of the light, E_x is the horizontal component, E_y is the vertical component, E_{45} and E_{-45} are components at 45 degrees and -45 degrees respectively, and E_{right} and E_{left} are the components of right handed and left handed circularly

polarized light [9]. In this way, the polarization of light that follows the director can be described, and φ and $d\varphi/dz$, which correspond to S_2 and S_3 respectively, can be calculated at each surface.

2.5 Azobenzene dyes

The addition of azobenzene dye to a liquid crystal sample has been shown to enhance the optically-induced reorientation of the director. In fact, when the liquid crystal sample is doped with azo-dye in concentrations of less than 1 percent by weight, photoexcitation reduces the Freédericksz threshold by as much as two to three orders of magnitude [10]. This is called the Jánossy effect, and it is accounted for in the Eq. 13 by the constant η, which can be either positive or negative.

It has been shown that this photoinduced enchnacement results from a net torque on the bulk liquid crystal due to interactions with the ground and excited state dye molecules [10] [11]. For azo dye, the stable trans form and the meta-stable cis form shown in the Figure 8, correspond to the ground and excited states respectively. When

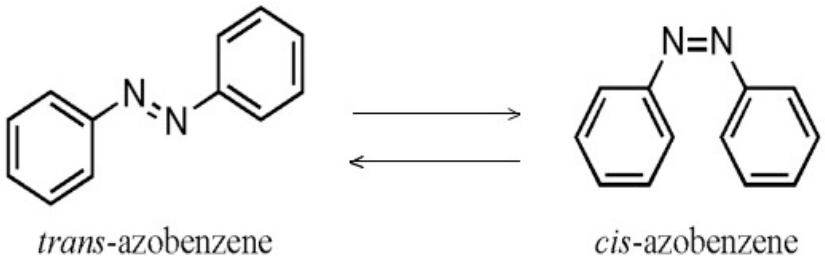


Figure 8: The molecular structure of a typical azo-dye showing both the trans- and cis-isomers.

the dye is irradiated with linearly polarized light of a certain wavelength, the molecules undergo several cycles of trans-cis isomerization. During this process, the dye molecules absorb the incoming light and are excited between trans and cis states. Rotation occurs

during each transistion eventually lining up the dye molecules perpendicular to the polarization of the applied light.

In a dye-doped LC sample, irradiation causes both the LC and dye molecules to rotate in the direction of the applied field. During the reorientation process, the LC molecules have a stronger attractive strength to the rod-like trans-isomers than to the bent cis-isomers. This attraction exerts the additional torque, accounted for by η, on the LC molecules during reorientation. Jánossy et al. demonstrated that the magnitude and the sign of the induced torque can depend on the relation of the molecular field strengths of the excited state and ground state molecules of the azo dyes [12].

The photoexcitation of the dye also alters the surface conditions in a liquid crystal sample. While the trans-isomers desorb from the polymer surface due to the attractive interactions with the liquid crystal, the cis-isomers adsorb to the polymer surface thus giving the sample unique surface conditions[13]. Upon irradiation, the dye molecules cycle between the trans- and cis-states depending on the energy absorbed. This affects the ratio of trans- to cis-states of the molecules in the sample thus altering the number of molecules bound to the polymer surface. As a result, the anchoring conditions change, which may contribute to a weakening of the anchoring energy at the surface [3][4].

Past research has examined the change in surface conditions due to photoexcitation [2]. The process involved orienting the LC from 0 to 45 degrees two times in order to see if the surface conditions had been altered. It was found that the LC took less time to reorient the second time when compared to the first, which suggests a change in surface conditions. This study calculates extrapolation lengths of azo-dye doped liquid crystals in the presence and absence of an optic field in order to confirm these results.

3 Theory

Jánnosy has shown, for the condition where $P \gg \lambda_0$, that light propagating through a sample exits with S_2 proportional to the director orientation, φ, and S_3 proportional to $(d\varphi/dz)/\Delta\varepsilon$[8]. From this, the second harmonic is given by the relationship,

$$S_2 = A\sin(2\varphi) \tag{22}$$

where A is a calibration constant [8]. For small φ Eq. 22 becomes

$$\varphi = c_2 S_2 \tag{23}$$

where $c_2 = 1/2A$ and φ is in radians. Once calibration of the second harmonic is complete, measurement of S_2 yields φ as shown by Eq. 23; that is, measurement of S_2 yields the orientation of the director.

Furthermore, the relationship for the first harmonic is given by

$$\varphi' = \Delta\varepsilon c_3 S_3 \tag{24}$$

where $\varphi' = d\varphi/dz$ and c_3 is a calibration constant. The constant c_3 is determined by exploiting the fact that $d^2\varphi/dz^2 = 0$ for Eq. 14 in the absence of a field. This gives Eq. 16 as the orientation of the director where $d\varphi/dz = k$. Therefore, the ratio of φ to $d\varphi/dz$ is just the thickness of the sample. As a result, the Stokes parameters can be related in the following way:

$$\frac{c_2 S_2}{c_3 S_3} = \Delta\varepsilon d \tag{25}$$

where d is the thickness of the sample. From this relation, c_3 can be determined by simply measuring the S_2 and S_3 in the absence of a field. With c_3, the measurement of S_3 yields φ' as shown by Eq. 24; that is, measurement of S_3 yields the change in the director per length z throughout the sample.

For small angles, Eq. 15 can be rewritten as

$$\varphi' = \frac{W_e}{K_2}(\varphi_e - \varphi) \tag{26}$$

which gives

$$\varphi = \varphi_e - \xi\varphi' \tag{27}$$

This suggests a linear relationship between φ and φ' with the extrapolation length ξ as the slope. Therefore, ξ is just the change in φ over the change in φ'.

A change in φ and φ' is brought about the the presence of a field. As a result, extrapolation length can be calculated by comparing φ and φ' in the presence and absence of a field. Thus, Eq. 27 becomes

$$\xi = \frac{\varphi_{on} - \varphi_{off}}{\varphi'_{off} - \varphi'_{off}} = \frac{c_2(S_{2,on} - S_{2,off})}{\Delta\varepsilon c_3(S_{3,off} - S_{3,on}).} \tag{28}$$

Now Eq. 28 holds for applied electric and magnetic fields, but is a problem for applied optical fields. Optical fields cause photoexcitation and isomerization of azo-dye, which impact the order of the nematic, namely the values of the dielectric anisotropy $\Delta\varepsilon$ and the twist constant K_2 [2]. For this reason, it is necessary to use a magnetic field to cause the change required to examine extrapolation lengths.

4 Methodology

4.1 Samples

Samples consisted of a dyed calamitic liquid crystal mixture contained between two rubbed, PI-coated pieces of glass. The calamitic liquid crystal E7 was prepared with either o-, m-, and p-methyl red, or DO3 dyes at concentrations of 0.10% (dye/liquid crystal) by weight. Cleaned glass slides were spin-coated with the polymer polyimide (PI) and uniformly rubbed with velvet in one direction to establish orientation. The rubbing strength was controlled using the apparatus shown in the Figure 9. The

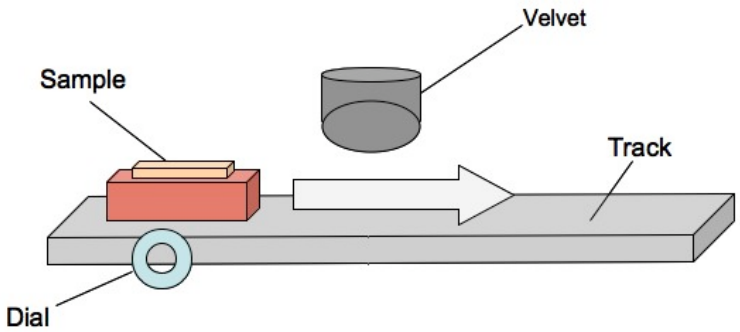


Figure 9: An illustration of the apparatus used to established rubbing strength on liquid crystal samples. Note that the dial controls the height of the track and therefore the amount of contact allowed on the sample.

strongest rubbing strength was established at a certain pressure, then medium and low rubbing strengths were established by lowering the contact point by a quarter-turn and half-turn respectively. Spacers between 10 and 50μm thick were placed between the glass slides. These slides were then filled with E7 mixture and sealed with slow drying epoxy.

4.2 Experimental Design

To induce a change in surface conditions, the dye-liquid crystal samples were re-oriented optically. This was done using a probe-pump system as shown in Figure 10. The system utilizes an Argon-ion pump laser tuned to 488-nm for photoexcitation of

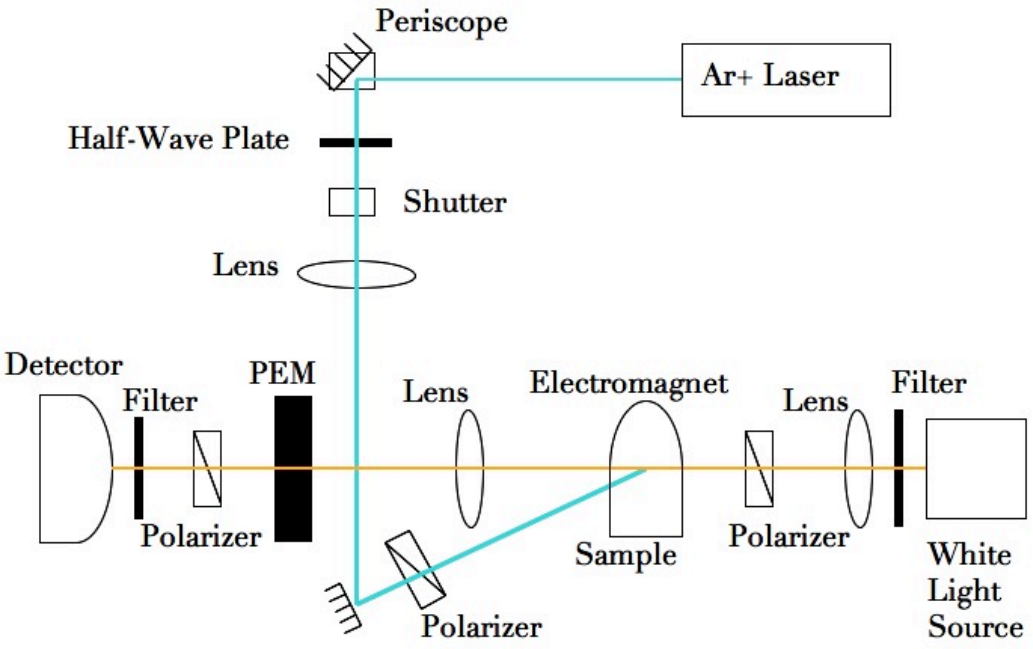


Figure 10: Experimental Set-up [2].

the dye and alignment of the sample. The pump intensity was controlled with a combination of polarizers and a half-wave plate, and a probe beam was used to follow the director throughout the reorientation.

A white light source was used for the probe beam because it is an incoherent light source that does not interfere with the components of the pump's optical field. The probe was polarized parallel to the rubbing direction on a sample to ensure a twist distortion. As mentioned in section 2.4, the polarization of light follows the director when the pitch of the twist distortion is much greater than the wavelength of light, $P \gg \lambda_0$ [1]. Since the pitch of the nematic is on the order of μm and the wavelength

on the order of nm, this condition is met for the sample. Therefore, as the pump beam induces reorientation, the vertically polarized probe beam exits the sample as linearly polarized light oriented parallel to the direction of the director.

This light travels through the photo-elastic modulator (PEM) and into the detector, which allows for measurement of φ and $d\varphi/dz$ at the surface. The filters were used to ensure accurate measurements, since they prevent the absorbtion of the probe beam by the sample and reduce any reflected pump-beam light away from the detector.

The PEM modulates the polarization of incoming light by passing light through a window made of quartz that oscillates at a frequency of 50kHz [8]. Because quartz is birefringent, the parallel and perpendicular components of light grow out of phase. The oscillation of the quartz amplifies the components of light making them easier to detect over the surrounding noise. The modulated light then passes through the detector whose signal is transferred to a lock-in amplifier. The lock-in amplifier serves to measure the phase shift between the components of light coming off the sample [14]. The knowledge of the phase shift δ allows for the components of the optic-field to be determined. These components are given as harmonics, where the second harmonic signal (SHS) gives the second Stokes parameter, S_2, and the first harmonic signal (FHS) gives the third Stokes parameter, S_3.

An electromagnet was used to observe the changes in surface conditions caused by the pump beam. The purpose of the electromagnet was to induce reorientation in a sample without altering the ratio of trans- to cis-isomers in the dye. In effect, the electromagnet kept the surface conditions constant as the sample was reoriented.

To calculate the initial extrapolation length of a sample, the magnet was turned on and off in the absence of the pump beam. Since the magnetic field was applied

perpendiculary to the director, the sample experienced a twist distortion when the magnet was turned on, which caused a change in S_2 and S_3. The change in the FHS and SHS was recorded and plugged into Eq. 28 to calculate the extrapolation length prior to irradiation.

To observe the changes in surface conditions, the extrapolation length was then calculated in the presence of an optic-field. The pump polarization was set to 90°, which aligned the sample vertically. Then the magnet was turned on and off, which induced a twist in the sample during irradiation. The change in S_2 and S_3 was measured again and Eq. 28 was used to calculate the extrapolation length of the sample in the presence of an optic field.

A sample holder was specifically designed to allow for both optic and magnetic field-induced reorientation. As shown by Figure 11, the apparatus utilized a thermoelectric cooler (TEC) system with specifications to fit between the poles of the magnet. The

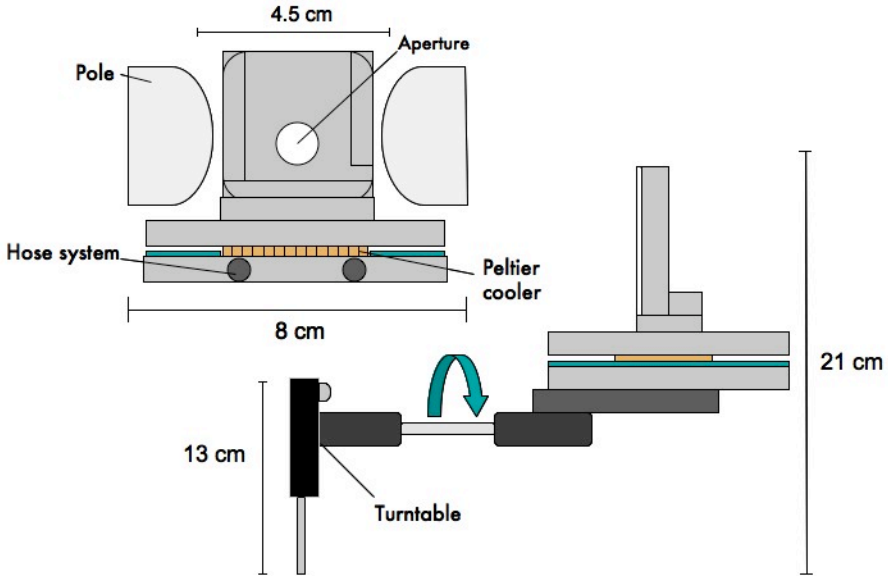


Figure 11: Sample holder for optic and magnetic field induced reorientation.

sample holder was constrained to hold a 3cm wide sample between the poles of the

electromagnet that had a maximum separation of 8cm. The idea was to minimze pole separation while allowing space for adjustments during calibrations. This resulted in a sample holder 4cm wide with a pole separation of 4.5cm. The holder was constructed with aluminum since it is a non-magnetic material with a low specific heat. An apeture 1cm in diameter was drilled to allow for the pump and probe beam to pass through the sample as shown in Figure 10.

A sensor was placed next to the sample to ensure the temperature remained between 20°C and 22°C, which is a sufficient temperature range for the nematic liquid crystal phase. The temperature was controlled with a peltier cooler that was placed underneath the sample holder between two pieces of alumninum 7cm wide. As current ran through the peltier cooler, it pumped heat from one side to the other creating one hot surface and one cold surface. In effect, heat was pumped away from the sample toward the bottom piece of alumnium containing the hose system. The hose system acted as a heat sink by continuously pumping water through the bottom piece of aluminum from a large reservoir. In order to work properly, the peltier cooler had to be in good thermal contact with the heat sink.

The TEC system was attached to a turntable 13cm high to allow the probe and pump beam to pass through the apeture unobscured. The turntable allowed the position of the sample to be adjusted between the poles of the magnet. It was especially useful when phase setting the lock-in amplifier and ensured accuracy during calibrations. For a complete outline of the experimental procedure, refer to Appendix C.

5 Results and discussion

The first component of testing examined the extrapolation length of samples in the absence of a pump beam. This was done by measuring the magnetic field-induced changes in FHS and the SHS with the pump beam turned off. The results are summarized in Table 1. The results for DO3 support what was anticipated. As the

Sample	$d(\mu m)$	χc_3 (rad/μm)	$c_2(S_{2,on} - S_{2,off})$	$(S_{3,off} - S_{3,on})$	$\xi(\mu m)$
DO3 (s)	35.5	-15.8	9.41×10^{-4}	-8.40×10^{-5}	0.711
DO3 (m)	41.1	-96.2	31.7×10^{-4}	-19.9×10^{-5}	0.165
DO3 (l)	31.1	-216	16.8×10^{-4}	-6.61×10^{-5}	0.118
m-MR (s)	27.3	-52.7	12.9×10^{-4}	-4.02×10^{-5}	0.606
o-MR (m)	28.0	-48.4	6.71×10^{-4}	-10.5×10^{-5}	0.131
p-MR (l)	29.0	-17.8	8.91×10^{-4}	-5.07×10^{-5}	0.988

Table 1: The calculated extrapolation length ξ in the absence of a pump beam.

rubbing strength increased, the extapolation length decreased. This confirmed the integrity of the rubbing process. When compared with MR, the ξ values for DO3 were smaller overall, which suggests that DO3 had a larger anchoring energy or a smaller twist constant K_2. Since previous data confirmed that MR reorients significantly more than DO3 in the same amount of time, the results were consistent. o-MR was most surprising because it had a much smaller extrapolation length than p- and m-MR that was more comparable to DO3.

The second component of testing examined the extrapolation length of samples in the presence of a pump beam. This was done by measuring the magnetic field-induced changes in the FHS and SHS with the pump beam turned on. The results are summarized in Table 2 and reveal a trend similar to Table 1.

DO3 still exhibited lower extrapolation lengths as rubbing strength increased and ξ values for MR were typically higher than DO3, but this time the ξ value for o-MR

Sample	$d(\mu m)$	χc_3 (rad/μm)	$c_2(S_{2,on} - S_{2,off})$	$(S_{3,off} - S_{3,on})$	$\xi(\mu m)$
DO3 (s)	35.5	-15.8	26.1×10^{-4}	-9.18×10^{-5}	1.81
DO3 (m)	41.1	-96.2	58.5×10^{-4}	-23.2×10^{-5}	0.261
DO3 (l)	31.1	-216	25.6×10^{-4}	-8.03×10^{-5}	0.147
m-MR (s)	27.3	-52.7	25.0×10^{-4}	-4.90×10^{-5}	0.968
o-MR (m)	28.0	-48.4	52.8×10^{-4}	-12.7×10^{-5}	0.854
p-MR (l)	29.0	-17.8	9.64×10^{-4}	-5.24×10^{-5}	1.03

Table 2: The calculated extrapolation length ξ in the presence of a pump beam.

appeared to be more consistent with p- and m-MR. It is also intereseting to note that DO3 small had a much higher extrapolation length than its DO3 counterparts.

The extrapolation lengths were then compared for samples in the presence and absence of the pump beam as shown in Table 3. According to the calculations, the ex-

Sample	$\xi_{before}(\mu m)$	$\xi_{after}(\mu m)$	$\Delta\xi(\mu m)$
DO3 (s)	0.711	1.81	1.099
DO3 (m)	0.165	0.261	0.096
DO3 (l)	0.118	1.47	1.352
m-MR (s)	0.606	0.968	0.362
o-MR (m)	0.131	0.854	0.723
p-MR (l)	0.988	1.03	0.042

Table 3: The comparison of the extrapolation lengths before and after pump irradiation where $\Delta\xi$ is the difference.

trapolation length appeared to change for each sample in the presence of a pump beam. Statistical analysis of the data confirmed this trend. A paired t-test was performed with a null hypothesis that the mean of the differences in extrapolation length does not differ from zero. The sample size (n) corresponded to the six calculated changes in extrapolation length, $\Delta\xi$, for each sample. The mean of these differences was 0.612 and the standard error of the differences was to 0.220, which yielded a t-value of 2.78. A two-tailed t-distribution for a t-value of 2.78 and 5 degrees of freedom (n-1) produced a P-value of 0.0387. Since $P < 0.05$, the null hypothesis had to be rejected, which led to the conclusion that the mean of the differences in extrapolation length differs

from zero. Thus, there was a statistical difference observed for extrapolation length in the presence and absence of an optic-field. It is interesting to note that the difference for each sample showed an increase in extrapolation length. This suggests that every sample experienced a weakening of anchoring energy at the surface or an increase in the twist constant K_2 in the presence of a pump beam.

As mentioned in section 3, the magnet was necessary because it kept surface conditions constant during reorientation. This effectively kept ξ constant because it did not impact the twist constant K_2 nor the anchoring coefficient W_e. As a result, Eq. 28 held in the presence of a magnetic field. However, as demonstrated, optical fields impact the surface conditions of a dye-doped sample, which results in a change in extrapolation length. Therefore, Eq. 28 does not hold for optical fields. In fact, when the pump-induced changes in S_3 and S_2 were evaluated in Eq. 28, negative extrapolation lengths were calculated as shown in Table 4. The results made no physical sense, so it was confirmed that Eq. 28 is not valid for optical reoreintation.

Sample	$d(\mu m)$	χc_3 (rad/μm)	$c_2(S_{2,on} - S_{2,off})$	$(S_{3,off} - S_{3,on})$	$\xi(\mu m)$
DO3 (s)	35.5	-15.8	58.2×10^{-4}	0.523×10^{-5}	-70.5
DO3 (m)	41.1	-96.2	329×10^{-4}	0.197×10^{-5}	-173
DO3 (l)	31.1	-216	187×10^{-4}	2.13×10^{-5}	-4.07
m-MR (s)	27.3	-52.7	8.65×10^{-4}	0.523×10^{-5}	-9.29
o-MR (m)	28.0	-48.4	66.6×10^{-4}	0.961×10^{-5}	-14.3
p-MR (l)	29.0	-17.8	23.6×10^{-4}	2.68×10^{-5}	-1.67

Table 4: The calculated extrapolation length ξ when Eq. 28 was used for an optic field turned on and off.

However, the very fact that negative values were calculated indicates a change in extrapolation length. To see this, assume that ξ is positive and changes in the presence

of a field; that is, assume $\xi_{on}, \xi_{off} > 0$ and $\xi_{on} \neq \xi_{off}$. Then Eq. 27 becomes

$$\frac{\varphi_{on} - \varphi_{off}}{\varphi'_{off} - \varphi'_{on}} = \frac{\xi_{off} - \xi_{on}(\frac{\varphi'_{on}}{\varphi'_{off}})}{1 - (\frac{\varphi'_{on}}{\varphi'_{off}})}. \tag{29}$$

Now to achieve the values calculated in Table 4, $\frac{\varphi_{on}-\varphi_{off}}{\varphi'_{off}-\varphi'_{on}} < 0$, which occurs for two possible cases. Case I is the condition where $\varphi_{on} > \varphi_{off}$ and $\varphi'_{on} > \varphi'_{off}$. For this case,

$$1 - (\frac{\varphi'_{on}}{\varphi'_{off}}) < 0, \quad \text{since } \varphi'_{on} > \varphi'_{off}$$

which gives

$$\xi_{off} - \xi_{on}(\frac{\varphi'_{on}}{\varphi'_{off}}) > 0, \quad \text{by hypothesis.}$$

Therefore,

$$\frac{\xi_{off}}{\xi_{on}} > \frac{\varphi'_{on}}{\varphi'_{off}}, \quad \text{since } \xi_{on}, \xi_{off} > 0.$$

Now because $\frac{\varphi'_{on}}{\varphi'_{off}} > 1$, it follows that

$$\frac{\xi_{off}}{\xi_{on}} > 1$$

Thus, $\xi_{off} > \xi_{on}$ for case I.

Now case II is the condition where $\varphi_{on} < \varphi_{off}$ and $\varphi'_{on} < \varphi'_{off}$. For this case,

$$1 - (\frac{\varphi'_{on}}{\varphi'_{off}}) > 0, \quad \text{since } \varphi'_{on} < \varphi'_{off}$$

which gives

$$\xi_{off} - \xi_{on}(\frac{\varphi'_{on}}{\varphi'_{off}}) < 0, \quad \text{by hypothesis.}$$

Therefore,

$$\frac{\xi_{off}}{\xi_{on}} < \frac{\varphi'_{on}}{\varphi'_{off}}, \quad \text{since } \xi_{on}, \xi_{off} > 0.$$

Now because $\frac{\varphi'_{on}}{\varphi'_{off}} < 1$, it follows that

$$\frac{\xi_{off}}{\xi_{on}} < 1$$

As a result, $\xi_{off} < \xi_{on}$ for case II. Thus, in either case, $\xi_{on} \neq \xi_{off}$ for the condition where $\frac{\varphi_{on}-\varphi_{off}}{\varphi'_{off}-\varphi'_{on}} < 0$. This result confirms that extrapolation length must change in order for Eq. 28 to yield negative values for ξ. For a complete depiction of the experimental data, refer to Appendix D.

6 Conclusion

This study examined the effects of an optic-field on azo-dye doped liquid crystal reorientation. Previous data anticipated that pump irradiation induced a change in surface conditions either by causing a gliding of the easy axis or a weakening of anchoring energy. This study specifically examined the effect of an optic field on anchoring energy by comparing the extrapolation lengths of sample in the absence and presence of an optic field. It was anticipated that anchoring energies would change at the surface due to the photoisomerization of the dye. The overall consensus of the experimental results supports the initial conjecture that optic-fields induce a change in surface conditions for azo-dye doped liquid crystals. It was found for all samples that the extrapolation lengths increased in the presence of an optic field, which indicates a change in the twist constant K_2 or a weakening of anchoring energy at the surface.

7 Future work

It was demonstrated that the extrapolation lengths for azo-dye doped liquid crystals change in the presence of an optic field. The experimental data suggests for all samples that the extrapolation length increased at the surface as a result of photoexcitation of the dye. It could be determined why the extrapolation lengths only seem to increase at the surface and why no case of an decrease in extrapolation length was recorded. Furthermore, a trend could be established between the type of dye used and the extent to which the extrapolation lengths change by performing more trials per sample.

References

[1] Collings Peter, and Michael Hird. *Introduction to Liquid Crystals: Chemistry and Physics*. Bristol, PA: Taylor & Francis Inc., 1997.

[2] Statman, D; Wozniak, K; and Potuzko, M.; "Anchoring strength of o-, m-, and p-methyl red dye doped nematics on rubbed and unrubbed polyimide surfaces," Proc. SPIE 8114, 81140C (2011)

[3] Komitov, L.; Ruslim, C.; Matsuzawa, Y.; and Ichimura, C.; "Photoinduced anchoring transitions in a nematic doped with azo dyes," *Liquid Crystals*, 27, 1011-1016 (2000).

[4] Ouchi, Y.; Feller, M.B.; Moses, T.; and Shen, Y.R.; "Surface memory effect at the liquid-crystal-polymer interface," *Phys. Rev. Lett.*, 68, 3040-3043, (1992).

[5] Collings, Peter. *Liquid Crystals: Natures Delicate Phase of Matter*. 2nd ed. Princeton, NJ: Princeton University Press, 2002.

[6] Rapini, A.; and Papoular, M. "Distorsion d'une lamelle nematique sous champ magnetique conditions d'ancrage aux parois", *J Phys. (Paris) Colloq.* 30, C4-54, (1969).

[7] DeGennes, P.G. and Prost, J.; *The Physics of Liquid Crystals, 2nd edition.*, Clarendn Press, Oxford, 1993.

[8] Jánossy, I., "High-precision measurement of azimuthal rotational for liquid crystals on solid substrates," *J. Appl. Phys.*, 98, 043523 (2005).

[9] Hecht, E; *Optics* 3rd ed. (Addison-Wesley, Reading Massachusetts, 1998).

[10] Jánossy, I.; Lloyd, A.D.; and Wherrett, B.S. "Anomalous optical Fréedericksz transition in an absorbing liquid crystal," *Mol. Cryst. Liq. Cryst.*, 179, 1-12 (1990).

[11] Paparo, D.; Marrucci, L.; Abbate, G.; Santamato, E.; Kreuzer, M.; Lehnert, P.; and Vogeler, T. "Molecular-Field-Enhanced Optical Kerr Effect in Absorbing Liquids," *Phys. Rev. Lett.*,78, 38-41 (1997).

[12] Jánossy, I. and Szabados, L. "Optical reorientation of nematic liquid crystals in the presence of photoisomerization," *Phys. Rev. E*, 58, 4598-4604 (1998).

[13] Ouskova, E.; Reznikov, Y.; Shiyanovskii, S.V.; Su, L; West, J.L.; Kuksenok, O.V.; Francescangeli, O.; and Simoni, F.; "Photo-orientation of liquid crystals due to light-induced desorption and adsorption of dye molecules on an aligning surface," *Phys. Rev. E*, 64, 051709 (2001).

[14] Scofield, John H. "Frequency-domain description of a lock-in amplifier." *American Journal of Physics* (AAPT) 62 (2): 129-133.

[15] Lagerwall, Jan and Giusy Scalia. "Applications of liquid crystals in soft matter nano-, bio-, and microtechnology." *Current Applied Physics* 12(6): 1387-1412 (2012).

Appendix A Euler-Lagrange derivation

$$F = \int_0^L [\frac{1}{2}\ K_2(\frac{\partial\varphi}{\partial z})^2 + \frac{1}{2}\eta\Delta\varepsilon\varepsilon_0\langle E^2\rangle \sin^2(\varphi-\varphi_E)]dz + \frac{1}{2}W_e \sin^2(\varphi-\varphi_e)$$

$$U = \frac{1}{2}K_2(\frac{d\varphi}{dz})^2 + \frac{1}{2}\eta\Delta\varepsilon\varepsilon_0\langle E^2\rangle \sin^2(\varphi-\varphi_E)$$

$$\frac{dF}{d\alpha} = 0$$

The distortion free energy F takes into account the energy from 0 to L due to the distortion of the director and the applied field; it also accounts for the anchoring energies at the surface. Therefore it follows that $\frac{dF}{d\alpha}$ is the derivative with respect to α of the energy from 0 to L and at the surface. Taking the derivative of the energy between 0 and L is tricky, so attention will be focused on its derivation:

$$\int_0^L \frac{dU}{d\alpha}dz = \int_0^L \frac{dU}{d\varphi}\frac{d\varphi}{d\alpha}dz + \int_0^L \frac{dU}{d(\frac{d\varphi}{dz})}\frac{d(\frac{d\varphi}{dz})}{d\alpha}dz$$

where

$$\int_0^L \frac{dU}{d(\frac{d\varphi}{dz})}\frac{d(\frac{d\varphi}{dz})}{d\alpha}dz = \int_0^L \frac{dU}{d(\frac{d\varphi}{dz})}d(\frac{d\varphi}{d\alpha})$$

which, with the help of integration by parts, is evaluated to yield

$$\frac{dU}{d(\frac{d\varphi}{dz})}\frac{d\varphi}{d\alpha}\Big|_0^L - \int_0^L \frac{d\left(\frac{dU}{d(\frac{d\varphi}{dz})}\right)}{dz}\frac{d\varphi}{d\alpha}dz.$$

With this result, it follows that

$$\int_0^L \frac{dU}{d\alpha}dz = \int_0^L \left[\frac{dU}{d\varphi}\frac{d\varphi}{d\alpha} - \frac{d\left(\frac{dU}{d(\frac{d\varphi}{dz})}\right)}{dz}\frac{d\varphi}{d\alpha}\right]dz + \frac{dU}{d(\frac{d\varphi}{dz})}\frac{d\varphi}{d\alpha}\Big|_0^L.$$

Now that the derivative from 0 to L has been determined, $\frac{dF}{d\alpha}$ can be calculated:

$$\frac{dF}{d\alpha} = \int_0^L \left[\frac{1}{2}\eta\Delta\varepsilon\varepsilon_0\langle E^2\rangle \sin[2(\varphi-\varphi_E)] - K_2\frac{d^2\varphi}{dz^2}\right]\frac{d\varphi}{d\alpha} + K_2\frac{d\varphi}{dz}\frac{d\varphi}{d\alpha}\Big|_0^L + \frac{1}{2}W_e \sin[2(\varphi-\varphi_e)]\frac{d\varphi}{d\alpha} = 0$$

By examining the left-hand side of the equation more closely, it reveals that the terms within the integral represent the Euler-Lagrange form of the energy U on a liquid crystal (without accounting for surface conditions), which is equivalent to nullity:

$$\frac{1}{2}\eta\Delta\varepsilon\varepsilon_0\langle E^2\rangle \sin[2(\varphi-\varphi_E)] - K_2\frac{d^2\varphi}{dz^2} = \frac{dU}{d\varphi} - \frac{d}{dz}\frac{dU}{d(\frac{d\varphi}{dz})} = 0$$

From this, it follows that the motion of the director in the bulk is given by

$$\frac{d^2\varphi}{dz^2} = \frac{1}{2}\eta\langle E^2\rangle\frac{\Delta\varepsilon\varepsilon_0}{K_2}\sin[2(\varphi-\varphi_E)].$$

Further integration of $d^2\varphi/dz^2$ is possible with the help of a simple mathematical trick. If both sides of the equation are multiplied by $\frac{d\varphi}{dz}$, each side becomes a perfect differential making the function easy to integrate:

$$\int\left[\frac{d^2\varphi}{dz^2}\frac{d\varphi}{dz}\right]dz = \int\left[\frac{1}{2}\eta\langle E^2\rangle\frac{\Delta\varepsilon\varepsilon_0}{K_2}\sin[2(\varphi-\varphi_E)]\right]d\varphi$$

is evaluated to yield

$$\frac{1}{2}(\frac{d\varphi}{dz})^2 = \frac{1}{2}\eta\langle E^2\rangle\frac{\Delta\varepsilon\varepsilon_0}{K_2}\frac{1}{2}[\sin^2(\varphi-\varphi_E)-\sin^2(\varphi_{max}-\varphi_E)]$$

which gives the equation

$$\frac{d\varphi}{dz} = \sqrt{\frac{\eta\Delta\varepsilon\varepsilon_0}{K_2}\langle E^2\rangle}\sqrt{\sin^2(\varphi-\varphi_E)-\sin^2(\varphi_{max}-\varphi_E)}.$$

It has been established that the left hand side of $\frac{dF}{d\alpha}$ is equivalent to nullity, which gives the right-hand side of the equation as

$$K_2\left(\frac{d\varphi}{dz}\right)\frac{d\varphi}{d\alpha}\Big|_0^L + \frac{1}{2}W_e\sin[2(\varphi-\varphi_e)]\frac{d\varphi}{d\alpha} = 0$$

which yields

$$\frac{d\varphi}{dz} = -\frac{1}{2}\frac{W_e}{K_2}\sin[2(\varphi-\varphi_e)]$$

at each surface of the liquid crystal sample.

Appendix B Sample preparation

Cleaning Glass Slides

1. Glass microscope slides are cut to specifications.
2. Glass slides are cleaned using Alconox.
3. The slides are placed in a 50mL beaker and separated by magnetic spacers.
4. The beaker is filled with DI water and placed into a Branson 2510 sonicator for 15 minutes.
5. Step 4 is repeated using 0.1M NaOH solution.
6. Step 4 is repeated using Isopropyl Alcohol.
7. Step 4 is repeated using DI water.
8. The slides are dried using pressurized nitrogen gas.

Making the Polyimide (PI) Solution

1. Combine 12mL of N-methyl-2-pyrrolidone and 3mL of toluene in a 50mL beaker.
2. Measure 5mL of PI-2555 in a 25mL graduated cylinder.
3. Add the solvent solution from Step 1 to the PI and stir.
4. Transfer the PI solution to a glass vial for storage.

Spin Coating

1. Clean slide pieces are placed one at a time onto spin coating device.
2. The motor is tuned to 40V for 1 minute to remove dust.
3. Polymer (PI) is applied to slides in a S-pattern using a pipette.
4. The motor is tuned to 40V for 4 minutes.
5. Excess PI is removed from the bottom of each slide piece with Isopropyl Alcohol on a cotton-tipped applicator.

PI Curing

1. Place slide pieces on tray with PI-side face up.
2. Place the tray into a Black and Decker toaster oven preheated to 90°C for 5 minutes.
3. Increase the temerature to 150°C for an additional 60 minutes.
4. Remove the slides from the oven.

Rubbing Samples

1. Place slide pieces PI-side up in the rubbing apparatus depicted in Figure 9.
2. Establish Large rubbing strength.

3. Carefully rub slides 3 times with velvet by pushing the platform along the track.
4. Establish Medium rubbing strength by lowering the track by a quarter-turn.
5. Repeat Step 3.
6. Establish Small rubbing strength by lowering the track by another quarter-turn.
7. Repeat Step 3.

Cell Assembly

1. Mylar sheets of a designated thickness are cut into long, thin strips to act as spacers in the cell.
2. The glass slides (one long piece, one short piece) are placed together with the PI sides facing inward and rubbing directions the same.
3. The sides of the sample are glued together using slow drying epoxy and allowed to dry.

Determination of Cell Thickness

1. Place cells into the spectrometer and take a transmittance spectrum.
2. The thickness of a cell is found by examining the the wavelengths of consecutive peaks in the spectrum through the follwing equation:

$$d = \frac{1}{2}\frac{\lambda_1\lambda_2}{(\lambda_1 - \lambda_2)}$$

3. The thickness d can be averaged by analyzing several pairs of consecutive peaks in the transmittance spectrum.

Filling Cells

1. Fill a pipette with the desired dye-doped liquid crystal.
2. Apply a small amount of the liquid crystal to the edge of the cell.
3. The cell will fill by capillary action.
4. Apply epoxy to the top and bottom edges of the cell and allow the epoxy to dry.
5. Check the integrity of the sample under a polarizing microscope.

Appendix C Experimental procedure

Experiment, Part I
To run part I of the experiment, turn ON:

- White light probe (set dial to 70)
- PEM
- Power Meter
- Temperature Control (TEC)
- LabView
- Lock-in Amplifier

Phase-Set the Lock-in Amplifier

1. Place sample into holder
   - Make sure the PEM is set at 0°
2. Set the sensitivity to the desired level
   - Keep the sensitivity level constant for the entire process
3. Adjust the signal on the Lock-in using the phase control buttons until the signal is close to 0 for the first harmonic (f) and the second harmonic (2f).
4. Rotate the PEM 1-2° and re-zero the signal for f and 2f using the phase control buttons.
5. Turn the phase up 90° for f and 2f, then set the PEM back to 0°.
6. Adjust the position of the sample using the holder's tilt controls until the signal for 2f is close to 0.
7. Zero the signal for f using the phase control buttons. Then turn the phase for f up 90°.
8. The system is now phase-set. Enter the phase for f and 2f into the Labview program at the appropriate sensitivity.

First and Second Harmonic Calibration:
As mentioned in section 3, the second harmonic (2f) gives the the second Stokes parameter, and the first harmonic (f) gives the third Stokes parameter. As shown by Jànnosy, the second Stokes parameter S_2 is proportional to φ by a calibration constant for the condition where $P \gg \lambda_0$. This relationship is given by

$$S_2 = A\sin(2\varphi_L) \approx 2A\varphi$$

where $2A = 1/c_2$. Since S_2 is measured by the second harmonic, the director orientation φ can be determined once c_2 is known.
A calibration test is run in order to determine c_2. To run a calibration test, the following steps are performed:

1. Phase-set the Lock-in Amplifier for a particular sensitivity.
2. Adjust the PEM through the cycle (φ =0°, +1°, +2°, 0°, -1°, -2°, 0°) while allowing LabView to record data between each movement.
3. Average the second harmonic (2f) signal recieved for each point in the PEM cycle. Then plot Signal vs. φ and add a trendline.
4. The slope of the trendline gives 2A in degrees. Convert 2A into radians and calculate c_2 from $c_2 = 1/2A$.

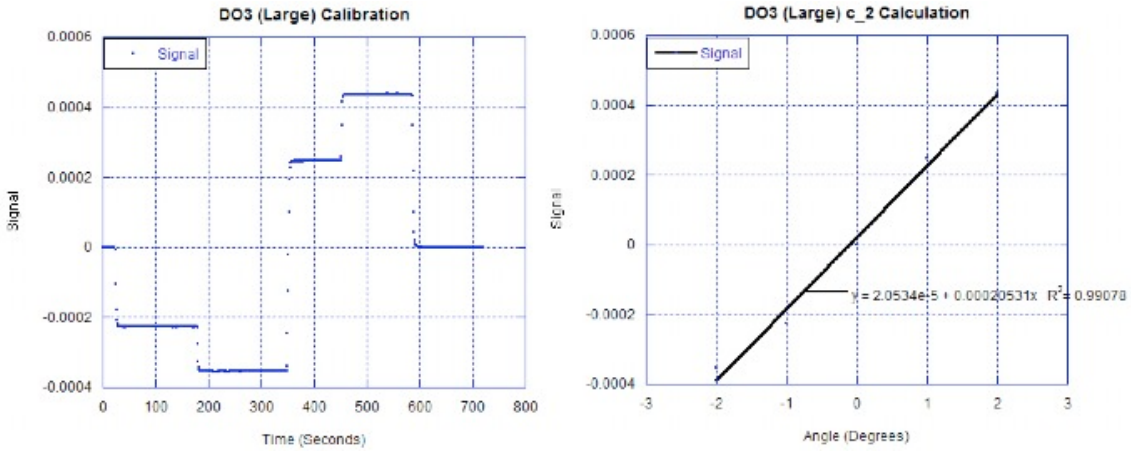


Figure C.1: An example of the method used to calculate c_2.

Jànnosy further showed that the third Stokes parameter S_3 is proportional to $(d\varphi/dz)/\Delta\varepsilon$ by a calibration constant c_3 for the condition where $P \gg \lambda_0$. As shown in section 3, this relationship becomes

$$\frac{c_2 S_2}{c_3 S_3} = \Delta\varepsilon d$$

in the absence of a field. Since the thickness of the sample d is determined interferometrically, c_3 can be calculated once c_2 is known and S_2 and S_3 are measured with the Ar^+ laser and electromagnet turned OFF.

Aligning the Ar^+ Laser

1. Put a laser block in front of the sample.
2. Turn on Ar^+ laser
   - Turn on Power Switch
   - Turn Key to ON
   - Discharge ON
3. Turn the shutter ON
4. Use the half wave plate to control the intensity of the pump beam.
5. Adjust the position of the pump using the mirror until the pump light is centered over the probe light.
6. Turn the shutter OFF, and return the laser to the desired intensity.

Experiment, Part II
To run part II of the experiment, turn ON:

1. Thermoflex 900 Temperature Control
    - Pressure: 0.3 bar- 3.5 bar
    - Flow Rate: $>$ 1 L/min (adjusted with control valve)
    - Temperature: 16 °C- 20°C
2. Electromagnet (Sorensen DLM series 600W control unit)
    - Max Continuous Power (water-cooled): 5.0A, 44V (0.22kW)

The purpose of experiment, part II is to determine how a sample responds under the influence of a magnetic field. For a perpendicualrly applied field, Jánossy has shown that the first harmonic signal (FHS) and the second harmonic signal (SHS) increase with field strength. Therefore, a sample's response to a field is determined simply by measuring the FHS and SHS throughout a range of field strengths.

$H(mT)$	$V(volts)$	$I(Amps)$
0-0.9	0	0
20	4.0	0.53
40	8.2	1.07
60	12.4	1.64
80	16.7	2.17
100	20.9	2.72
120	25.2	3.27
140	29.5	3.82
160	33.7	4.37
180	37.8	4.93
200	41.7	5.47

Table C5: The magnetic field values ranging from H=0.0-0.2 T and the corresponding VOLTAGE and CURRENT values for a pole separation of 4.5cm

A range of field values is provided in Table 1. The FHS and SHS are recorded at each value to see how the sample responds.

A typical sample response should look like the following:

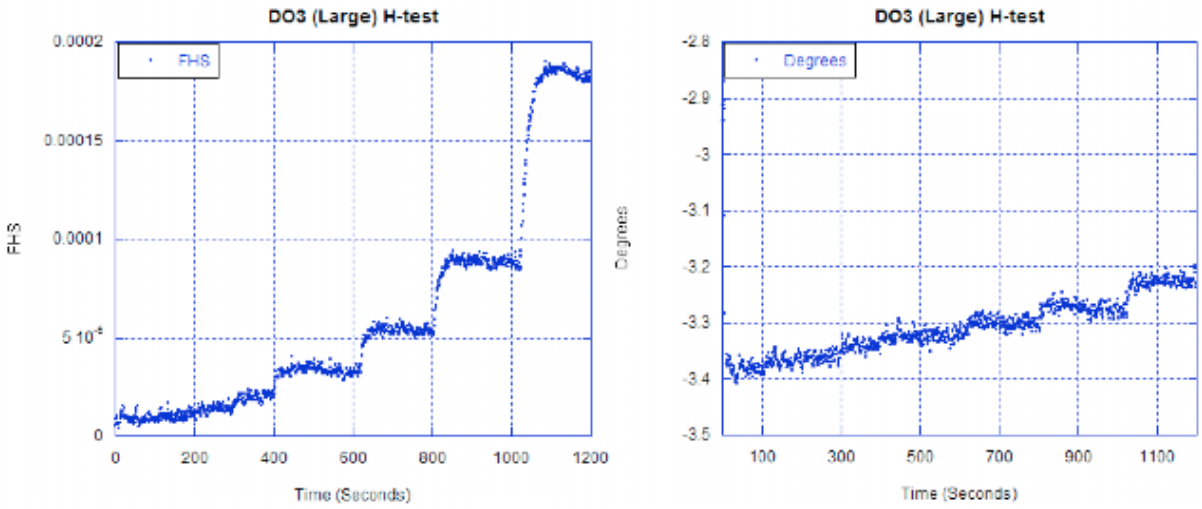


Figure C.2: A typical sample response to an increasing magnetic field.

Here, the field strength is increased over time. Note that the FHS and SHS increase with the field strength as anticipated. Weaker field strengths do not generate a strong response, but above a certain field strength the responses become more pronounced. This is evidence of the Freédericksz threshold and it typically occurs at a field strength of 0.08T for azo dye-doped samples. Once the FHS and SHS responses are recorded, adjust the magnet to a desired field strength (one above the Freédericksz threshold) and use the DLM control unit to turn the magnet output OFF.

Experiment, Part III

The purpose of experiment, part III is to determine the extrapolation length in the presence and absence of the pump beam. As shown in section 3, extrapolation length is given by

$$\xi = \frac{\varphi_{on} - \varphi_{off}}{\varphi'_{off} - \varphi'_{on}} = \frac{c_2(S_{2,on} - S_{2,off})}{\Delta\varepsilon c_3(S_{3,off} - S_{3,on})}.$$

Therefore, extrapolation length can be calculated by recording the change in the FHS and the SHS when the pump or magnet is turned on and off. The following process is used for determining extrapolation lengths:

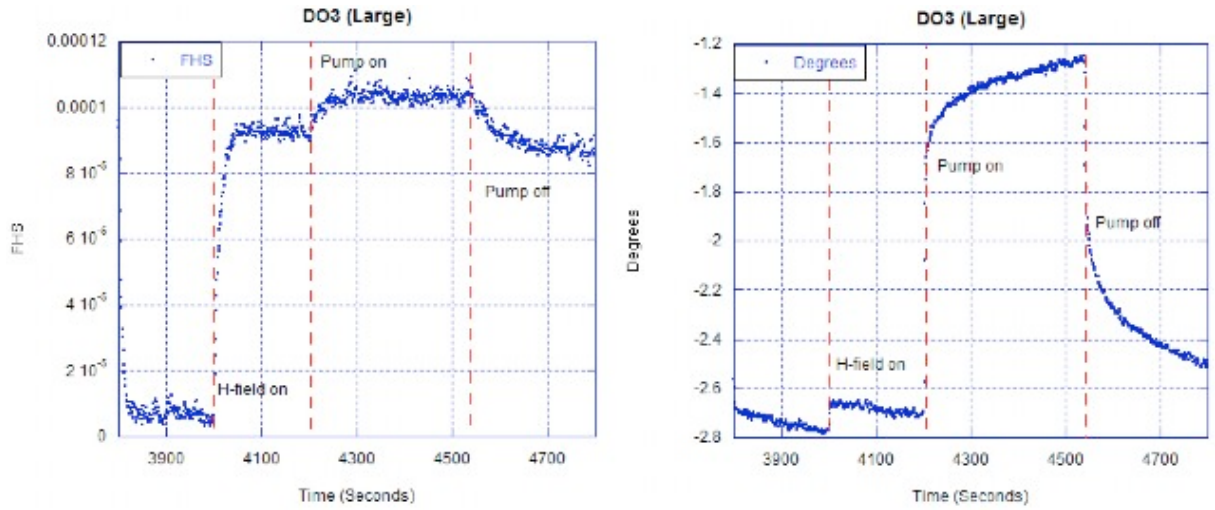


Figure C.3: A change in FHS and SHS induced by a magnetic field in the absense of the pump beam.

Note that the pump and the magnet are OFF initially. Then the magnet is turned on and a change is observed in the FHS and the SHS as shown in Figure C.3.

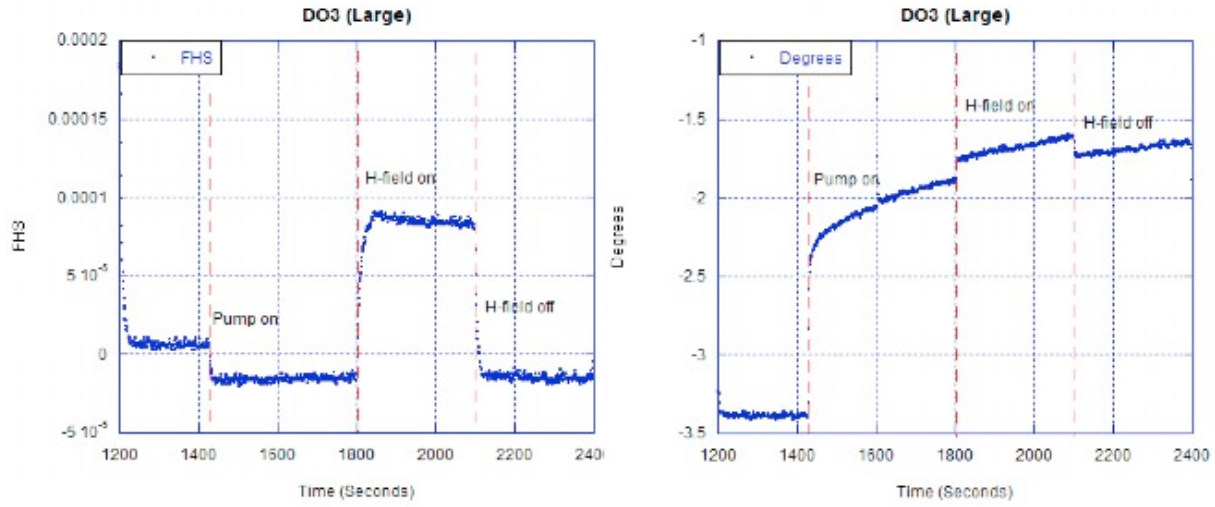


Figure C.4: A change in FHS and SHS induced by a magnetic field in the presence of the pump beam.

Next, the pump is turned on and the procedure is repeated as shown in Figure C.4. The changes are recorded and used to calculate the extrapolation length before and after pump irradiation. This was done by averaging fifty values of the FHS and the SHS before a change (S_2, off and S_3, off) and after a change (S_2, on and S_3, on) then plugging the values into the equation with the appropriate constants.

Appendix D Experimental Data

D.1 Results

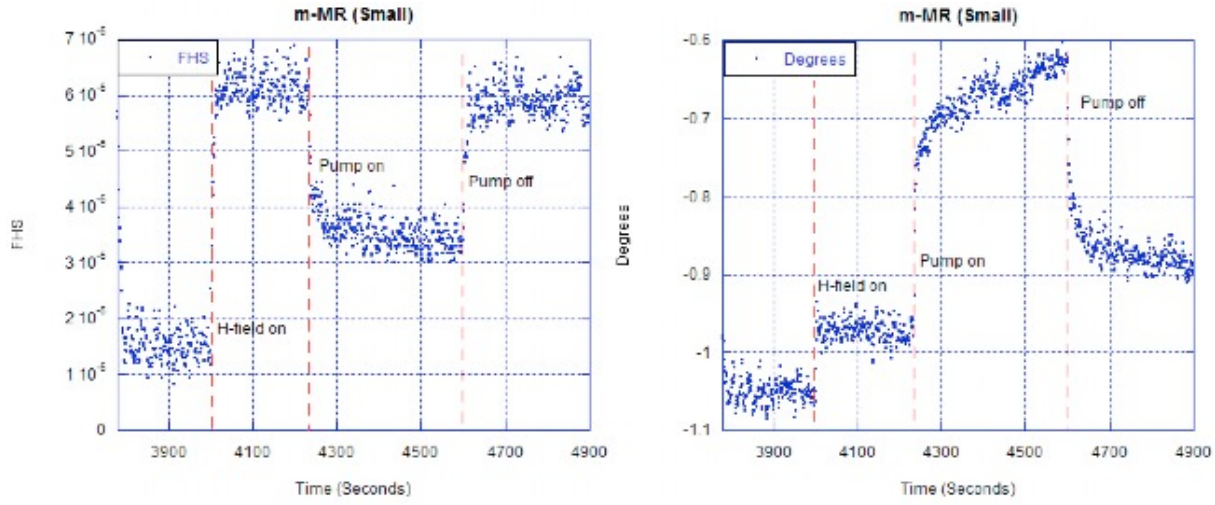


Figure D.1: The experimental results for m-MR. This section of data recorded FHS and SHS in the presence and absence of a magnetic field with the pump turned OFF. Note that the pump and magnet were initially OFF, and that the magnet was turned ON at 4000 seconds with a field strength of 0.14 T.

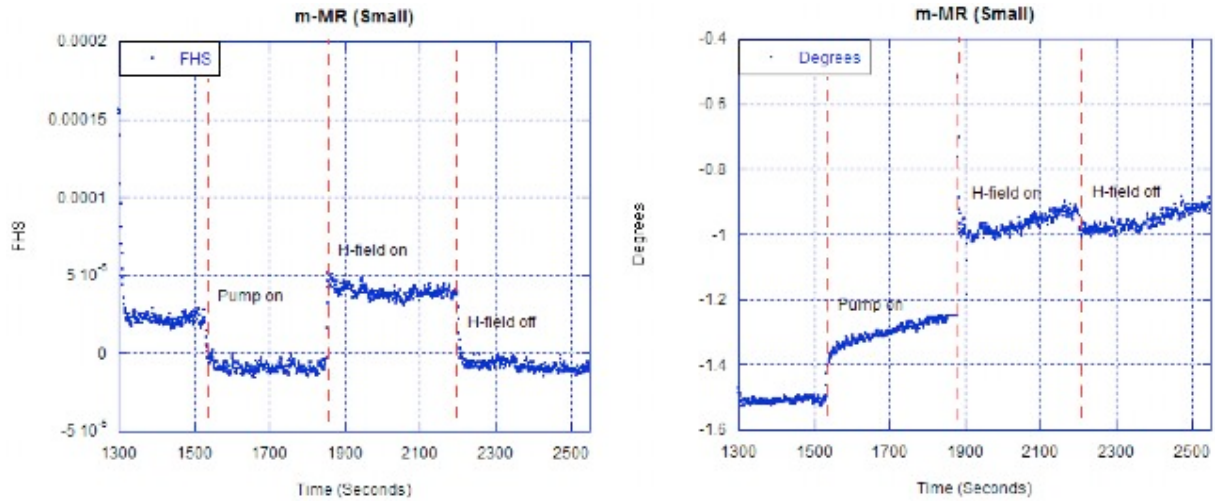


Figure D.2: The experimental results for m-MR. This section of data recorded FHS and SHS in the presence and absence of a magnetic field with the pump turned ON. Note that the pump was turned ON at 1530 seconds, and that the magnet was turned ON at 1850 seconds with a field strength of 0.14 T.

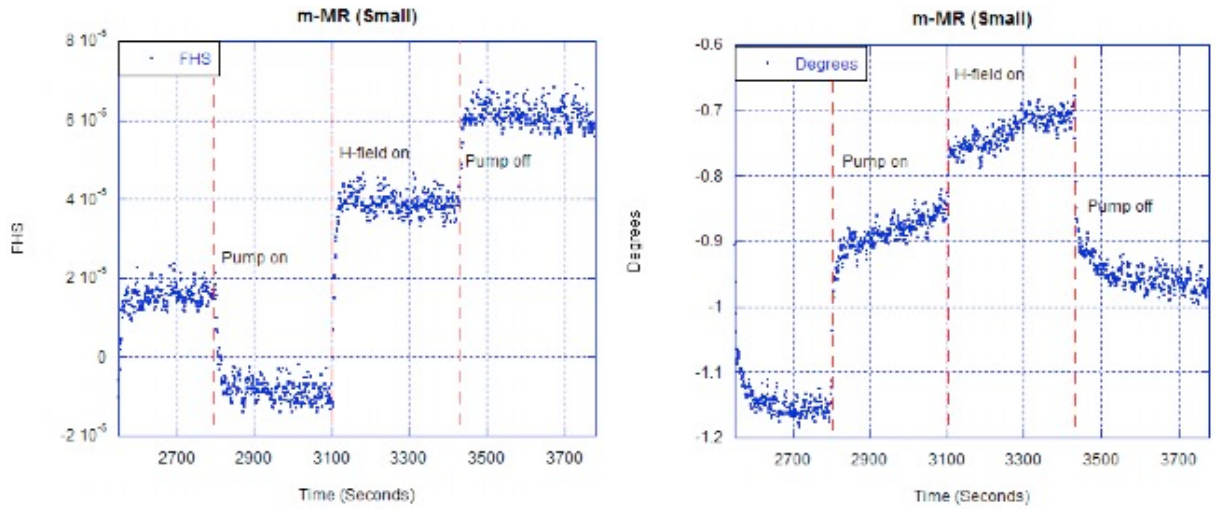


Figure D.3: The experimental results for m-MR. This section of data recorded FHS and SHS in the presence and absence of an optic field with the magnet turned OFF. Note that the pump and magnet were initially OFF, and that the pump was turned ON at 2800 seconds.

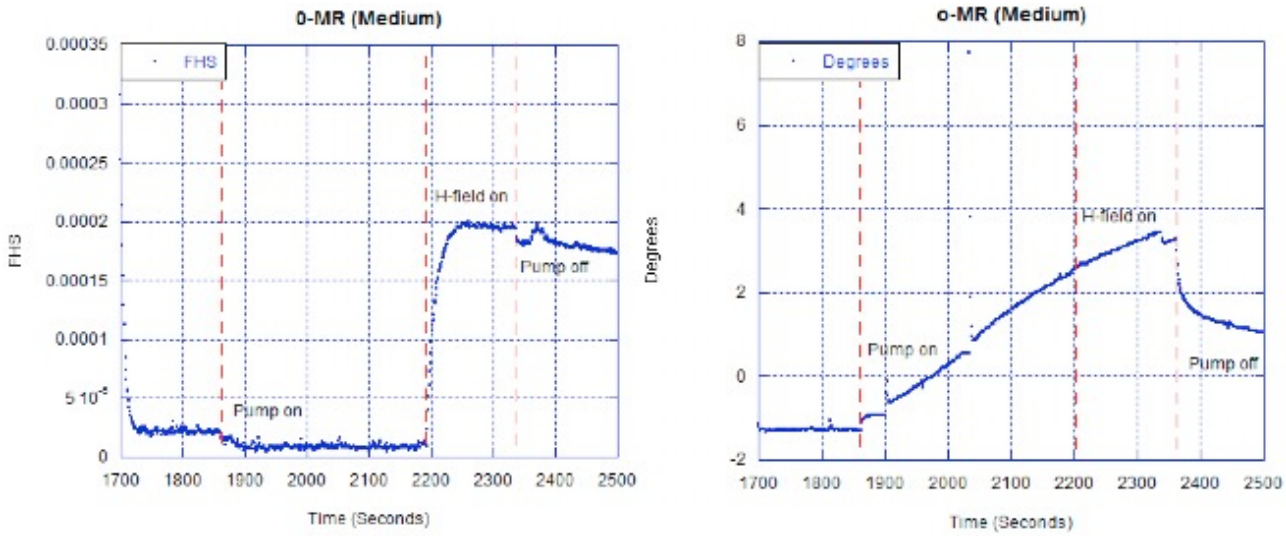


Figure D.4: The experimental results for o-MR. This section of data recorded FHS and SHS in the presence and absence of an optic field with the magnet turned OFF. Note that the pump and magnet were initially OFF, and that the pump was turned ON at 1860 seconds.

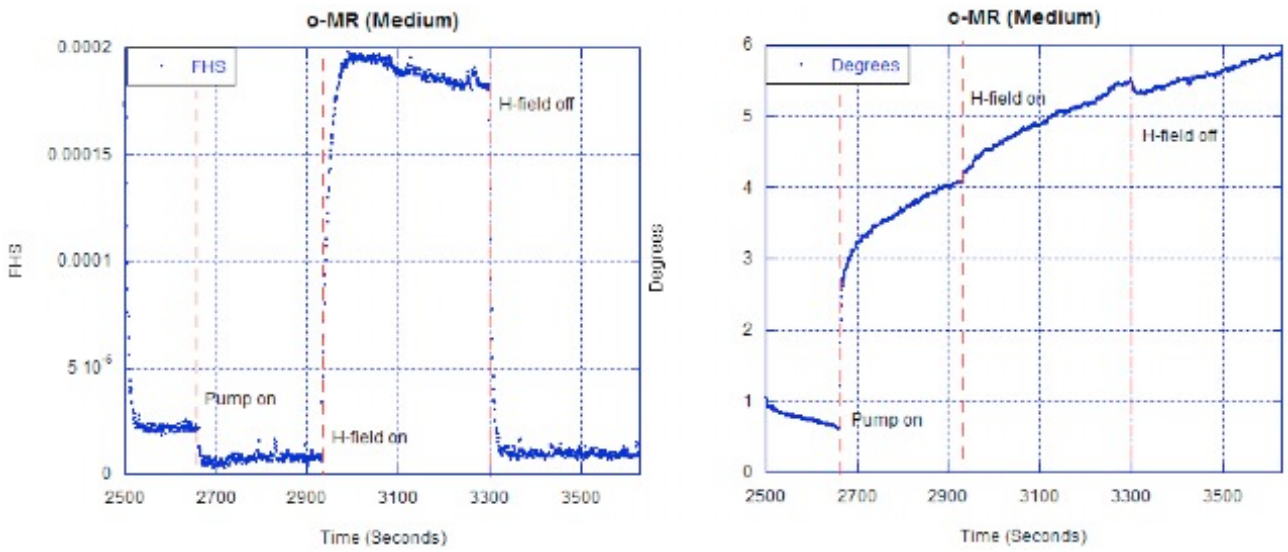


Figure D.5: The experimental results for o-MR. This section of data recorded FHS and SHS in the presence and absence of a magnetic field with the pump turned ON. Note that the pump was turned ON at 2660 seconds, and that the magnet was turned ON at 2930 seconds with a field strength of 0.14 T.

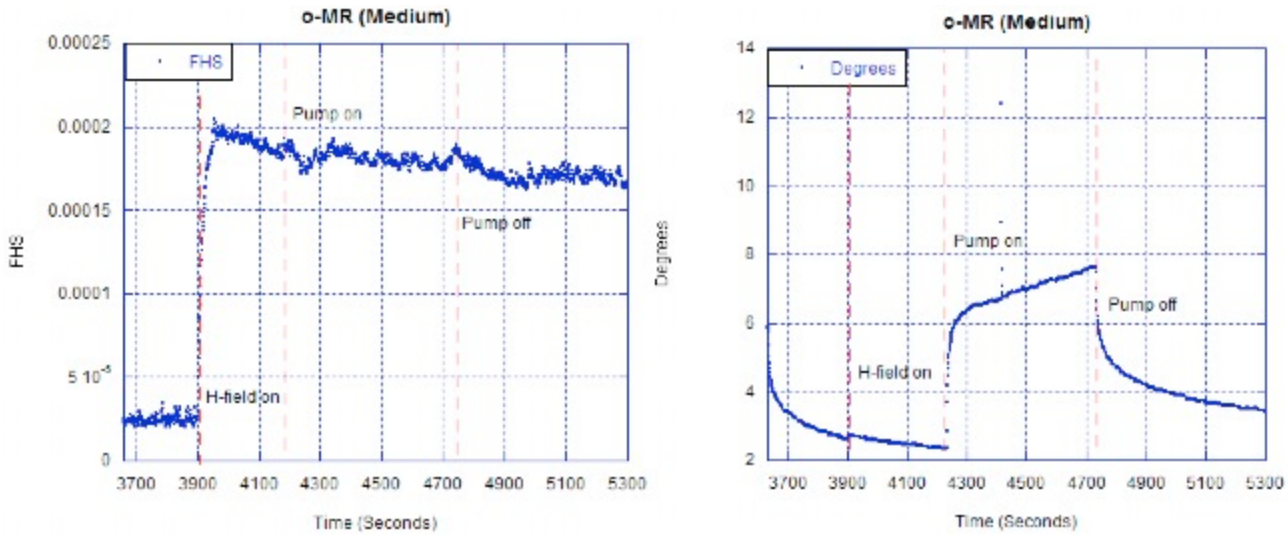


Figure D.6: The experimental results for o-MR. This section of data recorded FHS and SHS in the presence and absence of a magnetic field with the pump turned OFF. Note that the pump and magnet were initially OFF, and that the magnet was turned ON at 3900 seconds with a field strength of 0.14 T.

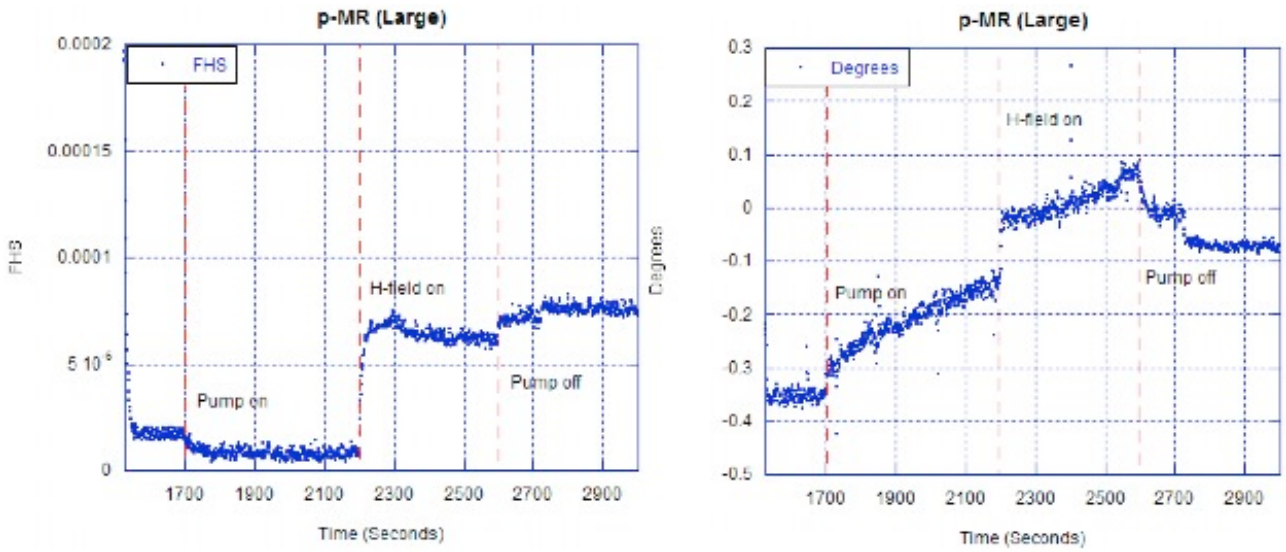


Figure D.7: The experimental results for p-MR. This section of data recorded FHS and SHS in the presence and absence of an optic field with the magnet turned OFF. Note that the pump and magnet were initially OFF, and that the pump was turned ON at 1700 seconds.

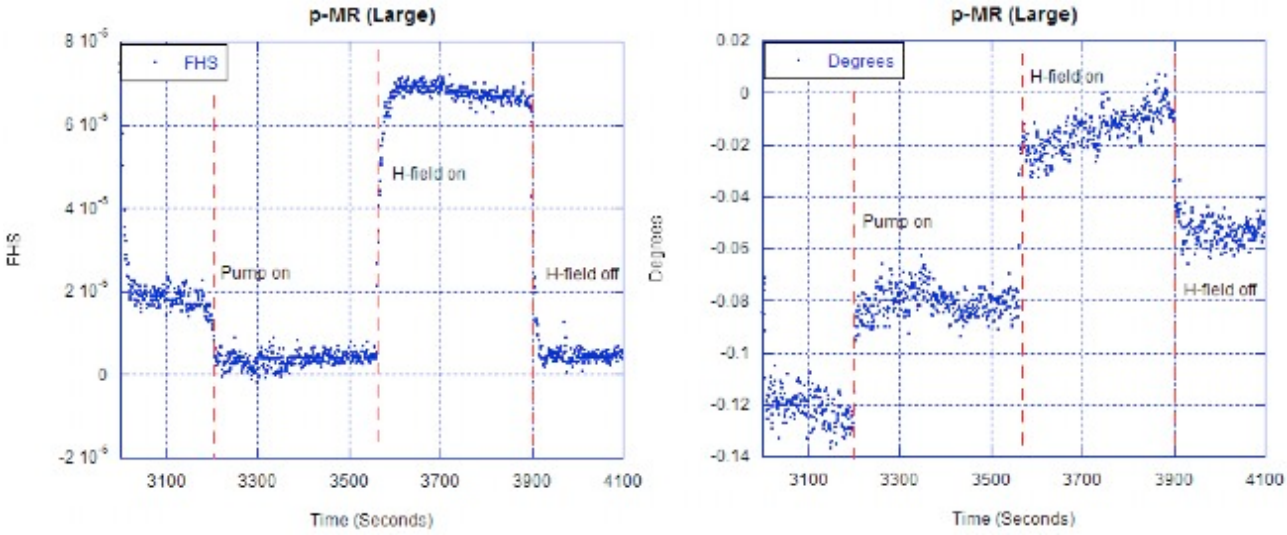


Figure D.8: The experimental results for p-MR. This section of data recorded FHS and SHS in the presence and absence of a magnetic field with the pump turned ON. Note that the pump was turned ON at 3200 seconds, and that the magnet was turned ON at 3560 seconds with a field strength of 0.14 T.

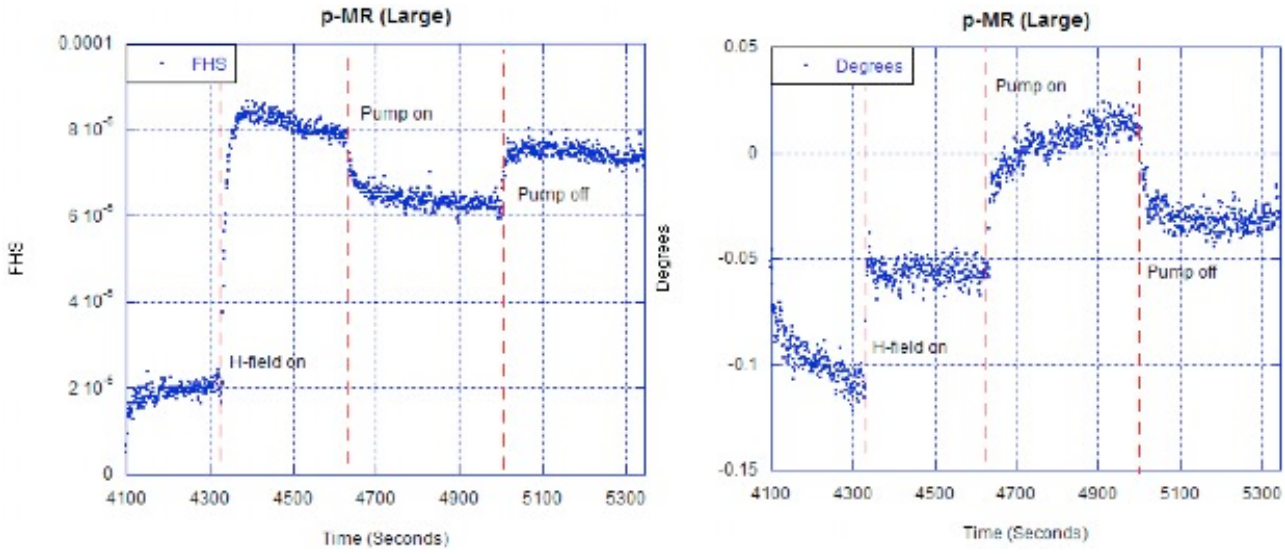


Figure D.9: The experimental results for p-MR. This section of data recorded FHS and SHS in the presence and absence of a magnetic field with the pump turned OFF. Note that the pump and magnet were initially OFF, and that the magnet was turned ON at 4330 seconds with a field strength of 0.14 T.

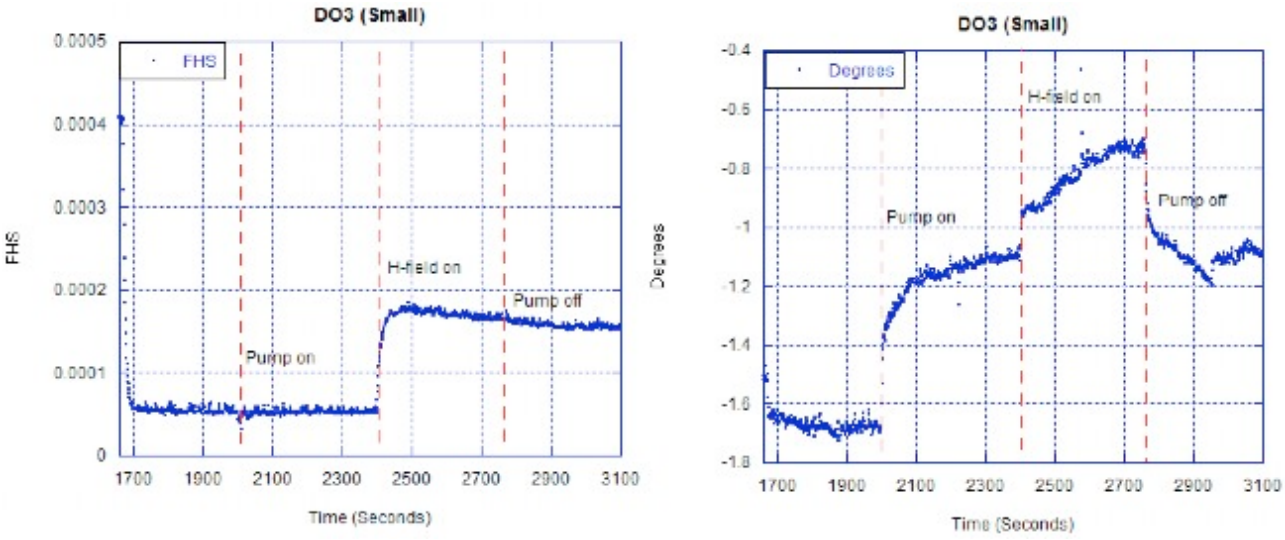


Figure D.10: The experimental results for DO3 (small). This section of data recorded FHS and SHS in the presence and absence of an optic field with the magnet turned OFF. Note that the pump and magnet were initially OFF, and that the pump was turned ON at 2000 seconds.

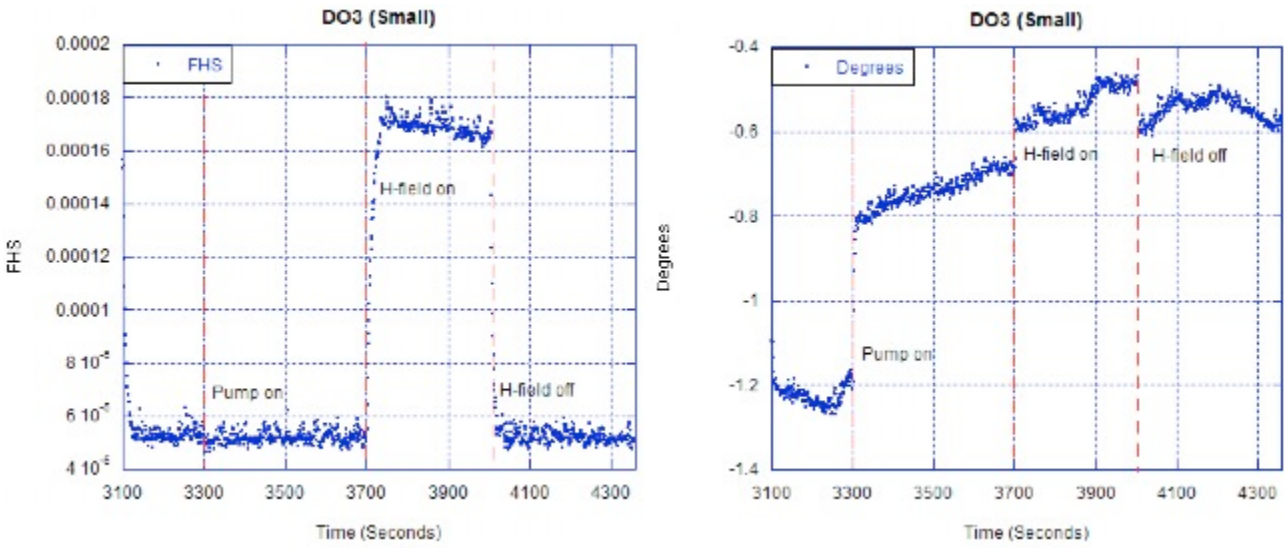


Figure D.11: The experimental results for DO3 (small). This section of data recorded FHS and SHS in the presence and absence of a magnetic field with the pump turned ON. Note that the pump was turned ON at 3300 seconds, and that the magnet was turned ON at 3700 seconds with a field strength of 0.14 T.

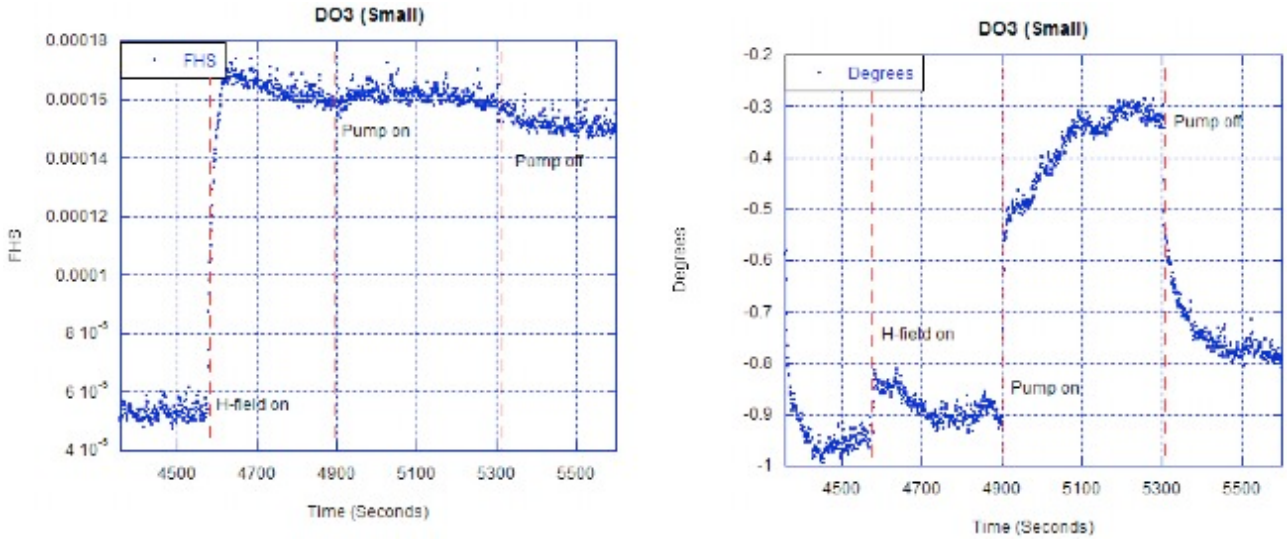


Figure D.12: The experimental results for DO3 (small). This section of data recorded FHS and SHS in the presence and absence of a magnetic field with the pump turned OFF. Note that the pump and magnet were initially OFF, and that the magnet was turned ON at 4600 seconds with a field strength of 0.14 T.

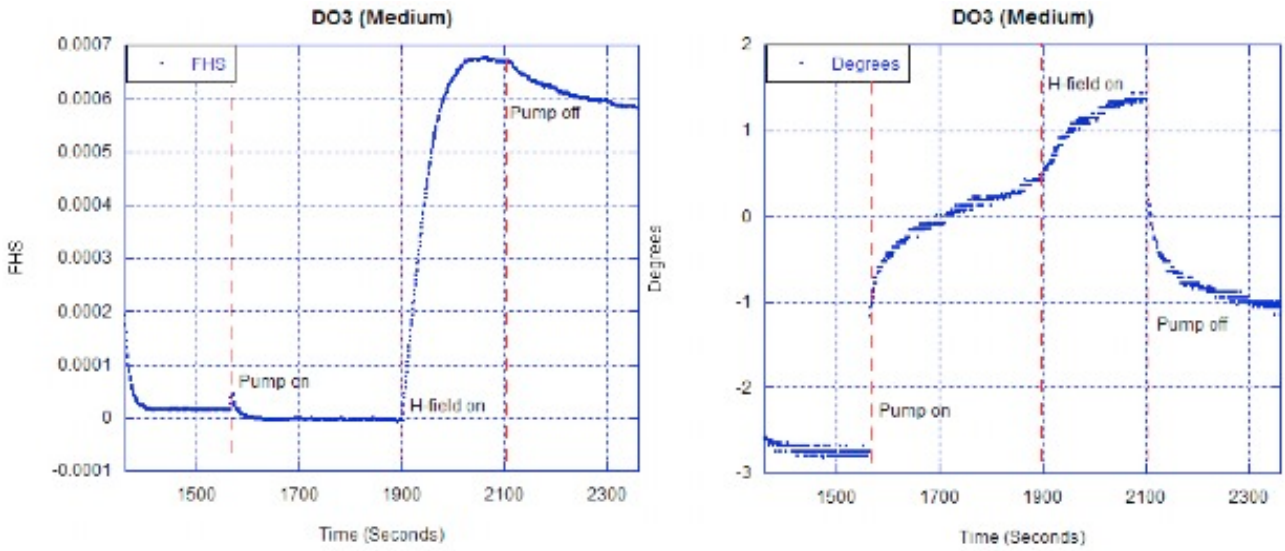


Figure D.13: The experimental results for DO3 (medium). This section of data recorded FHS and SHS in the presence and absence of an optic field with the magnet turned OFF. Note that the pump and magnet were initially OFF, and that the pump was turned ON at 1560 seconds.

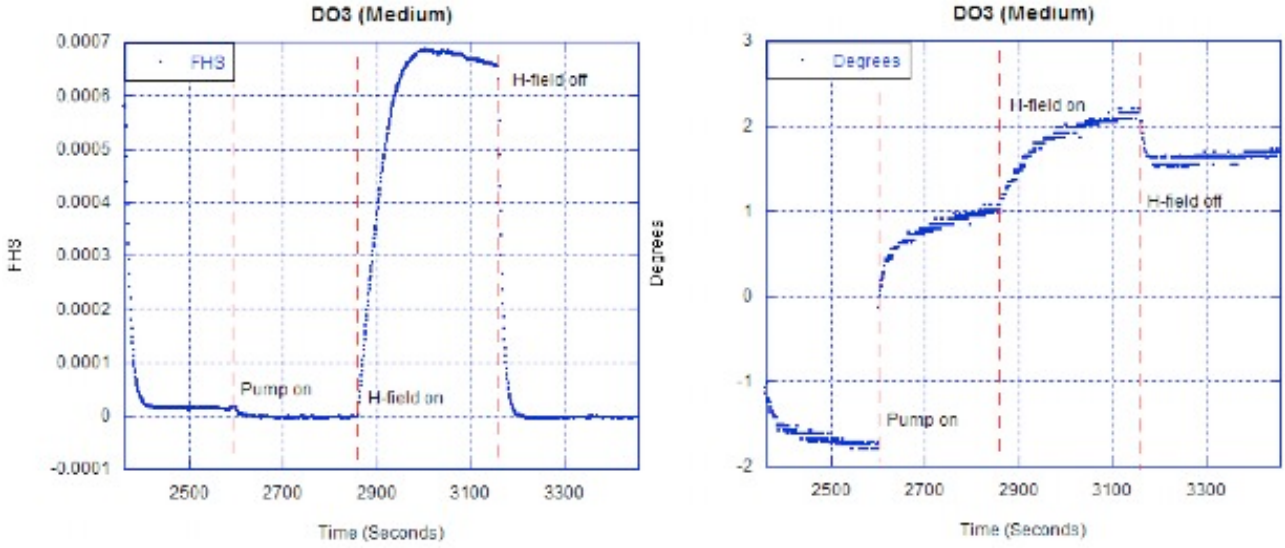


Figure D.14: The experimental results for DO3 (medium). This section of data recorded FHS and SHS in the presence and absence of a magnetic field with the pump turned ON. Note that the pump was turned ON at 2600 seconds, and that the magnet was turned ON at 2860 seconds with a field strength of 0.14 T.

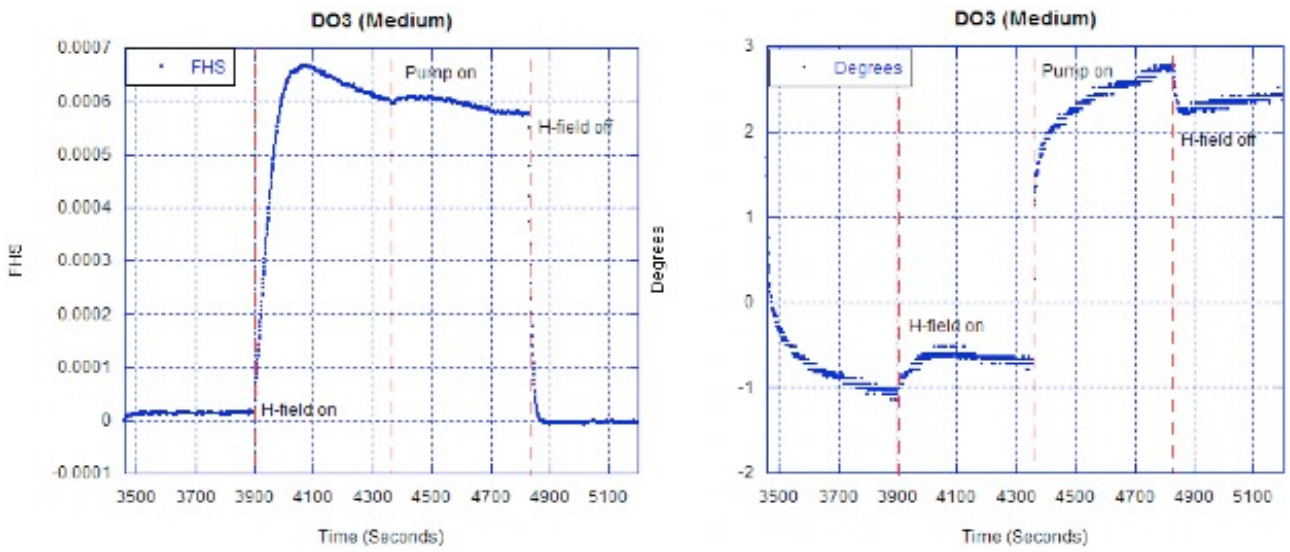


Figure D.15: The experimental results for DO3 (medium). This section of data recorded FHS and SHS in the presence and absence of a magnetic field with the pump turned OFF. Note that the pump and magnet were initially OFF, and that the magnet was turned ON at 3900 seconds with a field strength of 0.14 T.

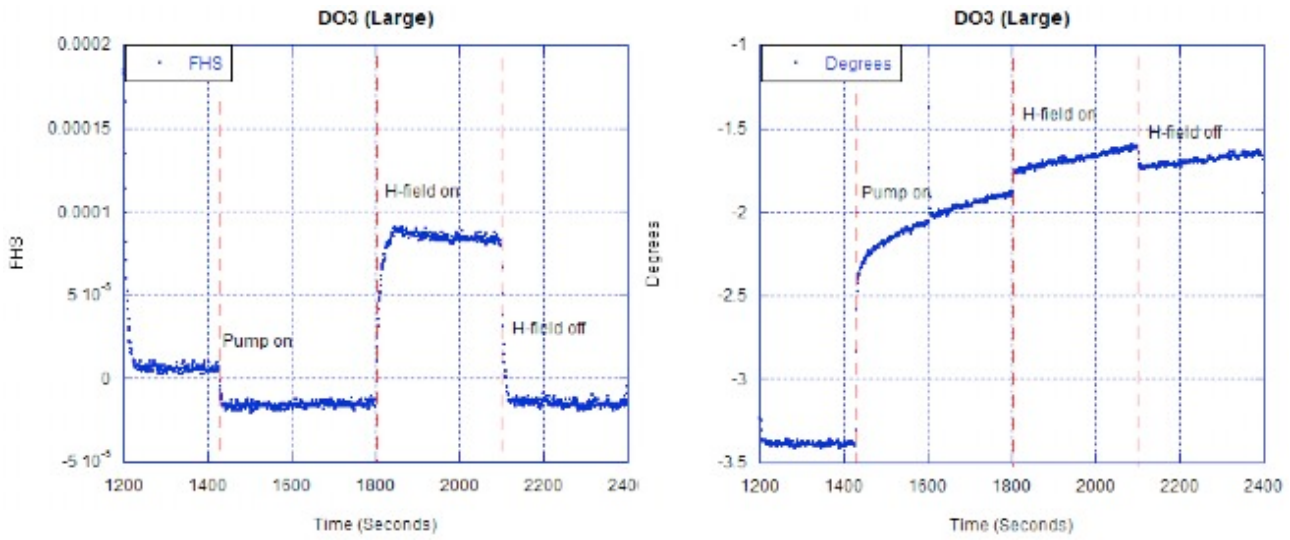


Figure D.16: The experimental results for DO3 (large). This section of data recorded FHS and SHS in the presence and absence of an optic field with the magnet turned OFF. Note that the pump and magnet were initially OFF, and that the pump was turned ON at 1430 seconds.

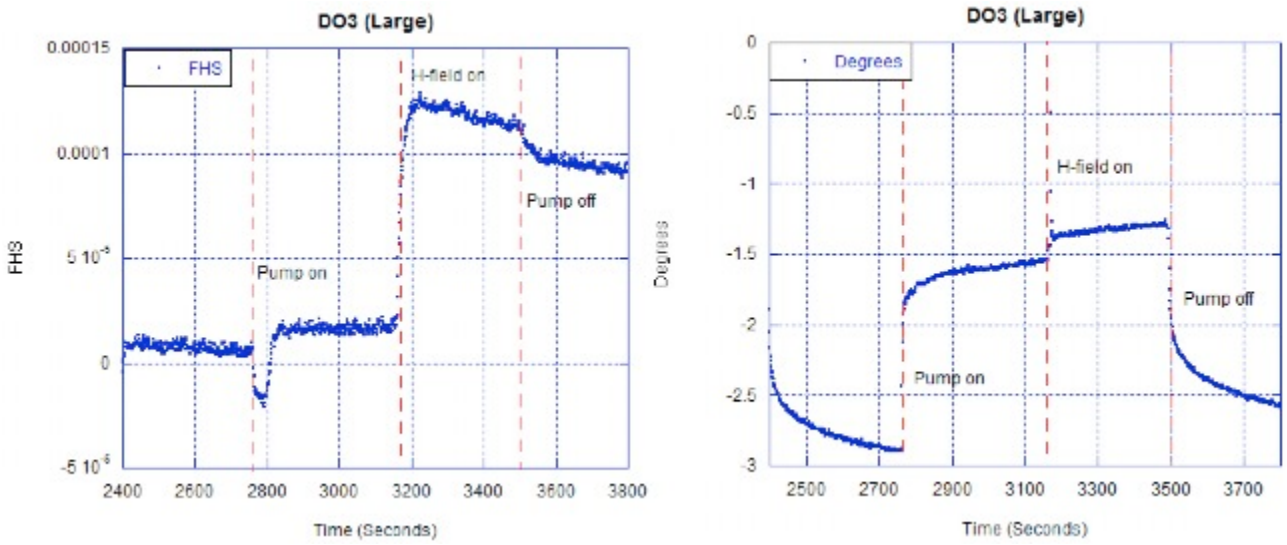


Figure D.17: The experimental results for DO3 (large). This section of data recorded FHS and SHS in the presence and absence of a magnetic field with the pump turned ON. Note that the pump was turned ON at 2760 seconds, and that the magnet was turned ON at 3160 seconds with a field strength of 0.12 T.

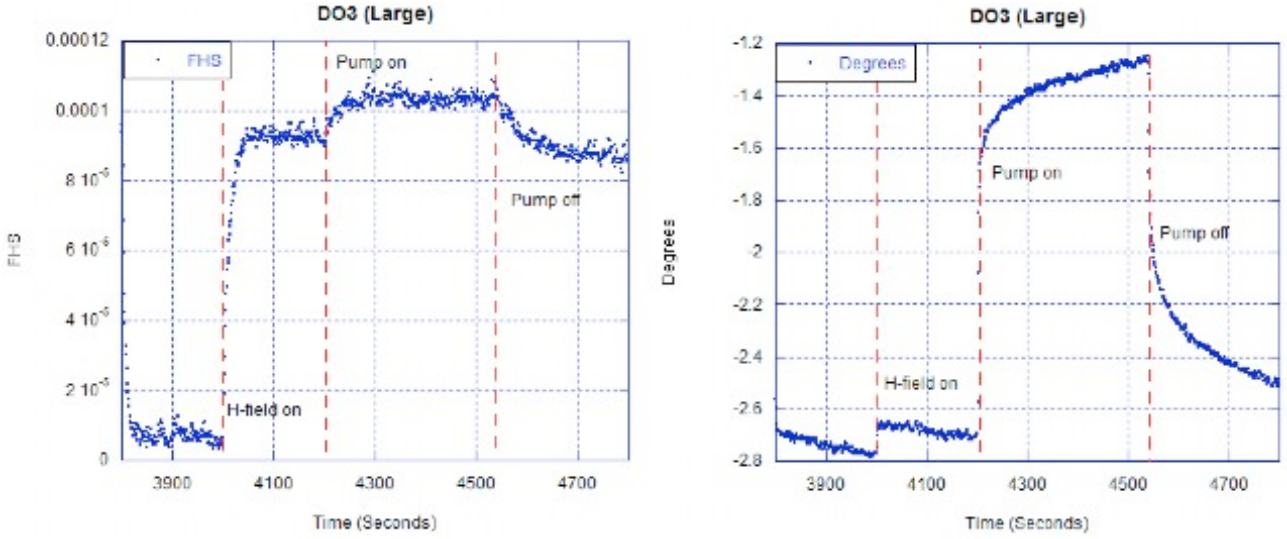


Figure D.18: The experimental results for DO3 (large). This section of data recorded FHS and SHS in the presence and absence of a magnetic field with the pump turned OFF. Note that the pump and magnet were initially OFF, and that the magnet was turned ON at 4000 seconds with a field strength of 0.12 T.

D.2 Calibrations

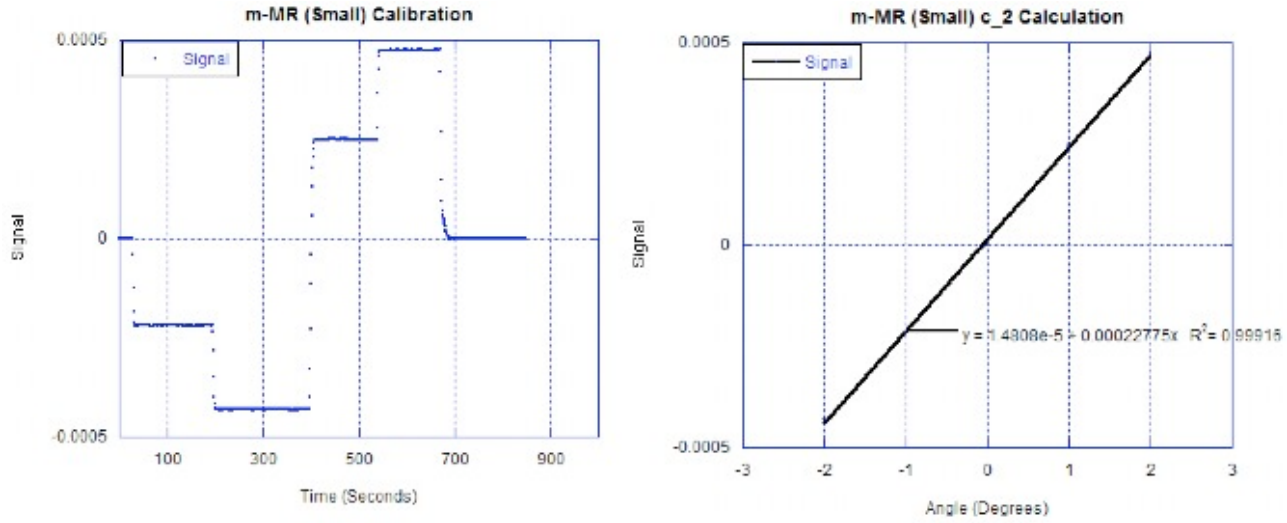


Figure D.19: The calibration test for m-MR and the corresponding relationship between the SHS and the Angle (Degrees). The calibration constant for this test was $c_2 = 76.6$ radians. Given the sample thickness $d = 27.3\mu m$, this yielded $\chi c_3 = -52.7$ radian/μm when S_2 and S_3 were measured in the absence of a field.

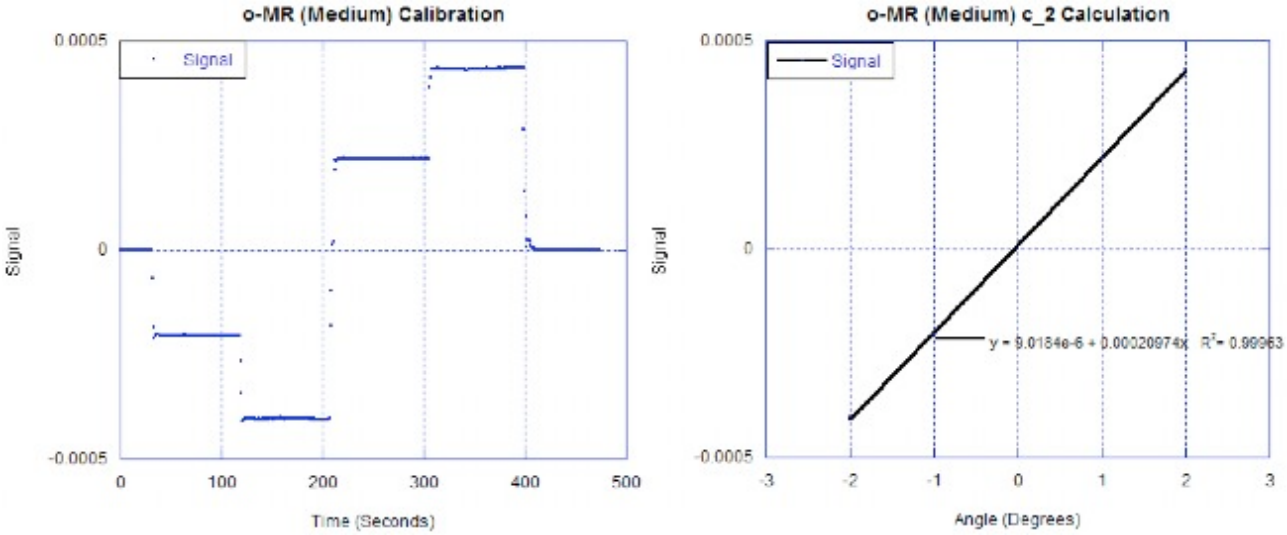


Figure D.20: The calibration test for m-MR and the corresponding relationship between the SHS and the Angle (Degrees). The calibration constant for this test was $c_2 = 83.2$ radians. Given the sample thickness $d = 28.0\mu m$, this yielded $\chi c_3 = -48.4$ radian/μm when S_2 and S_3 were measured in the absence of a field.

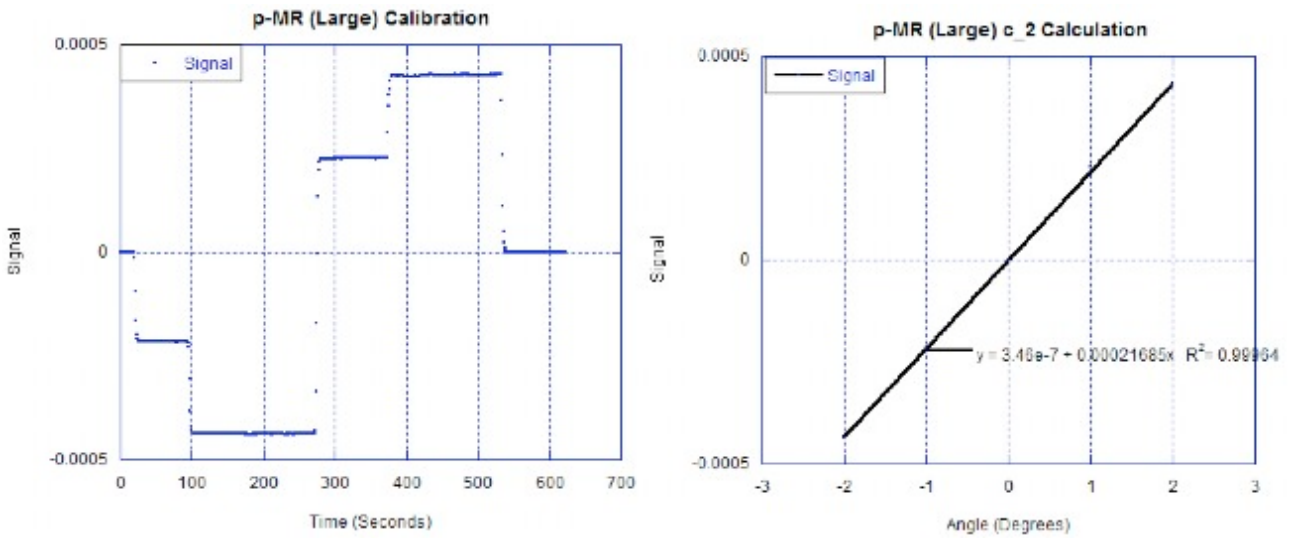


Figure D.21: The calibration test for m-MR and the corresponding relationship between the SHS and the Angle (Degrees). The calibration constant for this test was $c_2 = 80.5$ radians. Given the sample thickness $d = 29.0\mu m$, this yielded $\chi c_3 = -17.8$ radian/μm when S_2 and S_3 were measured in the absence of a field.

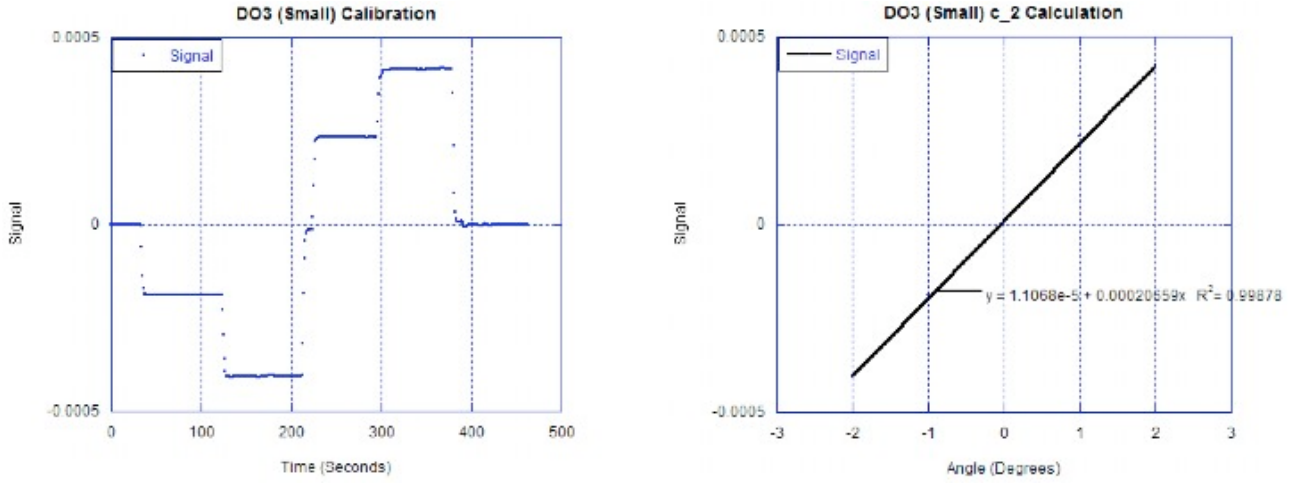


Figure D.22: The calibration test for m-MR and the corresponding relationship between the SHS and the Angle (Degrees). The calibration constant for this test was $c_2 = 84.4$ radians. Given the sample thickness $d = 35.5\mu m$, this yielded $\chi c_3 = -15.8$ radian/μm when S_2 and S_3 were measured in the absence of a field.

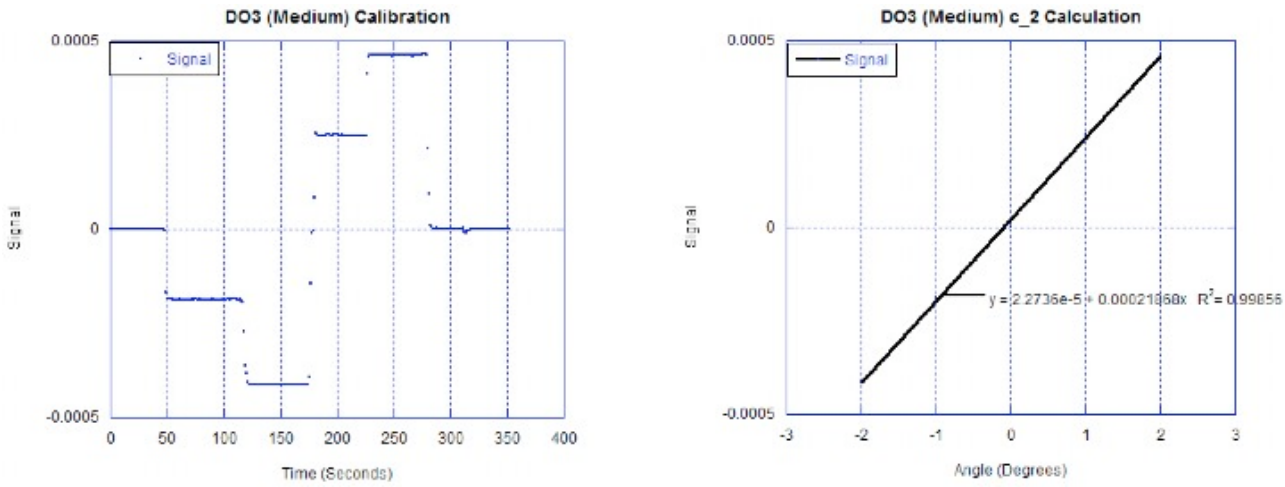


Figure D.23: The calibration test for m-MR and the corresponding relationship between the SHS and the Angle (Degrees). The calibration constant for this test was $c_2 = 79.8$ radians. Given the sample thickness $d = 41.1\mu m$, this yielded $\chi c_3 = -96.2$ radian/μm when S_2 and S_3 were measured in the absence of a field.

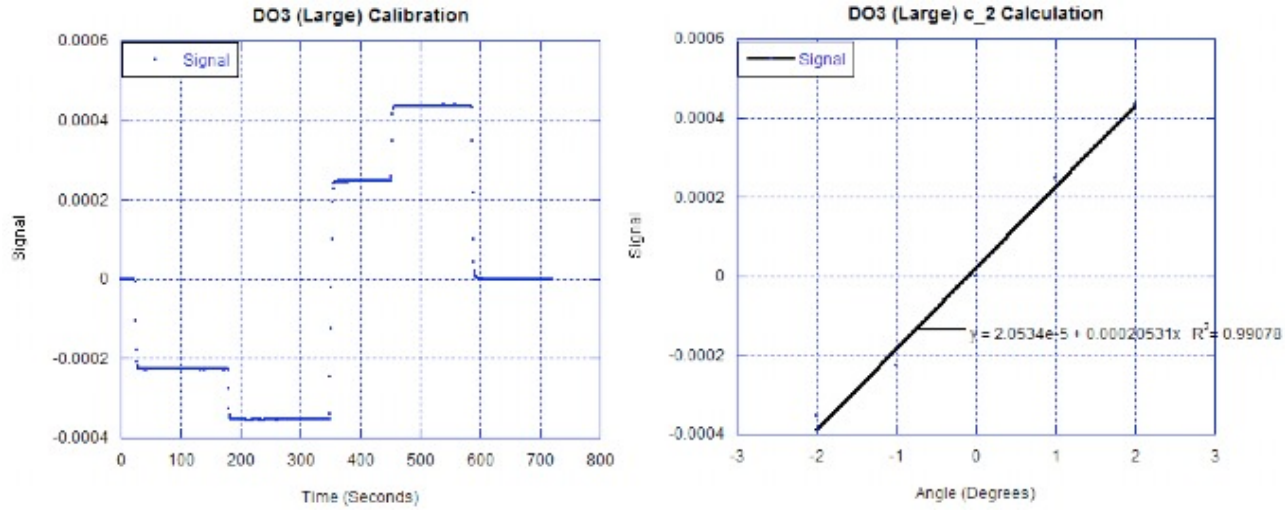


Figure D.24: The calibration test for m-MR and the corresponding relationship between the SHS and the Angle (Degrees). The calibration constant for this test was $c_2 = 85.0$ radians. Given the sample thickness $d = 31.1\mu m$, this yielded $\chi c_3 = -216$ radian/μm when S_2 and S_3 were measured in the absence of a field.